CHEMOTAXIS TOWARD AUTOINDUCER-2 AND ITS ROLE IN BIOFILM DEVELOPMENT IN *ESCHERICHIA COLI*

A Dissertation

by

SNEHA JAGDISH JANI

Submitted to the Office of Graduate and Professional Studies of
Texas A&M University
in partial fulfillment of the requirements for the degree of

DOCTOR OF PHILOSOPHY

Chair of Committee,	Michael Manson
Co-chair of Committee,	Arul Jayaraman
Committee Members,	Steve Lockless
	Paul Straight
Head of Department,	Thomas McKnight

May 2017

Major Subject: Microbiology

ABSTRACT

Bacteria navigate within their environment in response to gradients of several environmental cues, including nutrients, toxins, pH, temperature and oxygen. Recent studies demonstrate that *Escherichia coli* also senses signaling molecules, including the bacterial interspecies autoinducer-2 (AI-2). Such signals are likely to be encountered in the microenvironments inhabited by *E. coli* and can affect niche localization and colonization. AI-2 also affects biofilm formation and architecture in *E. coli*. In this study, I explore the role of AI-2 chemotaxis in biofilm formation. Using fluorescence microscopy and crystal violet assays for quantifying attached biomass, I show that, under static conditions, wild-type *E. coli* RP437 cells rapidly aggregate to initiate formation of surface-attached biofilms. Strains lacking either of the components required to sense AI-2, the binding protein LsrB and the chemoreceptor Tsr, make this transition at a slower rate. These results suggest that chemotaxis toward self-produced AI-2 enhances initial aggregation, thereby contributing to quorum-sensing dependent biofilm formation. In *in vitro* chemotaxis assays, the response to an external AI-2 gradient is independent of self-produced AI-2. Furthermore, cells require a very small amount of LsrB (~ 50-70 molecules per cell) to exhibit this response. These results suggest that cells are able to respond to non-self AI-2 without requiring induction of the AI-2 uptake system, which only occurs at higher cell density. In conclusion, our results suggest that

AI-2 chemotaxis allows *E. coli* to swim to an AI-2 source generated by the same or other species, to aggregate at that source, and to initiate biofilm formation.

ACKNOWLEDGEMENTS

I thank my committee chair, Michael Manson, for his guidance and support throughout the course of my PhD. He has given me the freedom to explore and learn from my experiences and has helped me become an independent scientist. He has been more than an academic advisor and has taught me several things about life in general. We have been through several professional and personal ups and downs and I am glad to have shared them all with him. I am also thankful to Mike for selecting me to be his teaching assistant through these years and hone my communication skills through it. I have also learned a lot from his exemplary teaching style and can only aspire to emulate it.

My committee co-chair, Arul Jayaraman, has been being very kind and supportive through difficult times, and I thank him for generously welcoming me into his lab. He has encouraged me to explore several areas of scientific research that allowed me to learn new things and also to develop personal and professional relationships with some wonderful individuals. Thanks also go to my committee members, Steve Lockless and Paul Straight, for providing the necessary outsiders perspective on my research work. They are great role models for the kind of academic scientists one should aim to be. Steve has been the voice of reason throughout my career, and I appreciate his taking the time to mentor me. I would also like to thank the Biology department, and specifically Arne Lekven and Jennifer Bradford, for providing me with a teaching assistant position and helping me deal with tough situations.

Andrew Seely and I collaborated to work on different aspects of this project. His ability to stay positive throughout has been helpful and motivating. I appreciate his contributions to this work. I would also like to thank Bill Cohn, Louis Morgan, and Attikos Hutras for their support.

I am grateful to Yufang Ding, Sasikiran Pasupuleti, and Nandita Kohli for helping me successfully transition into working in Arul Jayaraman's lab. I have learned a lot from them, both inside and outside the lab, and cherish the friendship we have developed over the years. Nitesh Sule and Rani Menon have been very encouraging, and I am thankful for all the scientific and non-scientific conversations we have had over the years. They have motivated me to aim higher and be better at everything I do.

Kunal Jani, Josiah Manson, Lance Brockway, Quint Peabody, and Clint Cheng all served as great peer models who taught me about dedicating oneself to one's passion, persevering through hard times, and being disciplined and competitive.

I would not be here without the support of my mother, Sunitta Jani. I am thankful to her for the years of hard work she put into providing me with a good life and nurturing me into becoming an assertive, independent individual. I am thankful to my father, Jagdish Jani, for teaching me the importance of developing a social life and enjoying things outside of work. He has also taught me the importance of taking risks and embracing both favorable and unfavorable consequences.

Lastly, I thank all my friends and extended family members who have provided me with love and support that has helped me stay sane through the course of my PhD.

CONTRIBUTORS AND FUNDING SOURCES

Contributors

My committee chair, Michael Manson, and co-chair, Arul Jayaraman, conceived this project and guided me through it.

Gregory Reinhart allowed me to work in his lab and to learn how to purify proteins from Robert Koenig, which made all the immunoblotting experiments in this study possible.

My colleague, Andrew Seely, and undergraduate researcher, Attikos Hutras, performed the capillary assay experiments that feature in Chapters II and III of my dissertation.

George Peabody for writing the Matlab code that I used for quantification of aggregates in the images.

Funding Sources

This work was made possible in part by the National Science Foundation under grant number 1121916 awarded to Michael Manson, Gregory Reinhart, and Arul Jayaraman. The Bartoszek Fund for Basic Biological Science Research provided funding to Michael Manson and contributed to the execution of this work.

TABLE OF CONTENTS

Page

LIST OF FIGURES

Page

LIST OF TABLES

Page

CHAPTER I

INTRODUCTION

I.1 Aim and Scope of the Study

Motile bacteria navigate their environment using a two-component phosphorelay system that couples the stimulus generated by sensing a ligand to the direction of flagellar rotation. This behavior is termed chemotaxis. The chemosensory network in *E. coli* has long served as a model for understanding signal transduction and response regulation in bacteria. In recent years, there has been increasing interest in understanding how this organism couples chemotaxis responses to biological signals found in the microenvironments it inhabits with behaviors such as biofilm formation and virulence. The main aim of this study is to understand the role of chemotaxis toward a specific environmental cue, autoinducer-2 (AI-2), in *E. coli* biofilm formation.

AI-2 is a bacterial interspecies quorum-sensing (QS) molecule. It is synthesized primarily during active growth as part of the activated methyl cycle that is present in both Gram-positive and Gram-negative bacteria. As it is produced by a multitude of organisms, it is present within numerous environments, including the intestines of warm-blooded mammals, which is a primary niche of *E. coli* (4-6). The presence of an intact AI-2-dependent QS system has been shown to affect energy-intensive group behaviors such as biofilm development in non-pathogenic *E. coli* species (7, 8) and virulence gene expression and attachment to epithelial cells in pathogenic enterohaemmorhagic *E. coli* (EHEC) (9, 10). AI-2 is also a chemoattractant for both pathogenic and non-pathogenic

E. coli (9, 11). As AI-2 affects cell density-dependent collective behaviors and because cells swim toward it, I hypothesized that chemotaxis toward AI-2 contributes to the initiation and establishment of biofilm communities. Understanding the influence of AI-2 chemotaxis on collective behaviors may allow the development of potent therapeutics to combat biofilm formation and reduce infection by pathogenic or opportunistic *E. coli*.

I.2 Quorum Sensing

Several environmentally relevant behaviors, such as biofilm formation, adhesin production, toxin secretion and motility are energy intensive, and bacteria invest resources in them only when cells are present in sufficient numbers (reviewed in refs. (12-16)). Both Gram-positive and Gram-negative bacteria use chemical signal-mediated 'quorum sensing' to determine the population density of the surrounding microbial community. These signals, called autoinducers, are constitutively produced and secreted by cells. They are present at low concentrations at low cell densities and at high concentrations at high cell densities. Synthesis of some autoinducers is under positive feedback control. Thus, as the density of the bacterial population increases, autoinducer production increases as well. Upon reaching a threshold, autoinducers bind to cell surface receptors and induce downstream signal transduction pathways that lead to population-wide changes in gene expression. These changes affect various aspects of cell physiology and behavior (Figure 1) (17).

Most known autoinducers are produced and recognized only by members of the same, or closely related, species. These molecules are used for intraspecies

communication and regulate species-specific behaviors. For example, Gram-negative bacteria such as *Pseudomonas aeruginosa* produce and recognize specific acyl homoserine lactones (AHLs) that allow them to regulate behaviors such as biofilm formation and virulence factor production within their host, whereas Gram-positive bacteria such as *Bacillus subtilis* use oligopeptides to regulate competence and sporulation (13, 15, 18).

In 1997, Bassler *et al* (19) discovered that the *Vibrio harveyi* autoinducer AI-2 regulates bioluminescence via a second QS pathway that is not restricted to this species. The supernatants of cultures of unrelated species, including *Yersinia enterocolitica* and *E. coli*, induce bioluminescence in *V. harveyi*. This study was the first to suggest that AI-2 is probably an interspecies signal. AI-2 has since been studied in several organisms, and a number of attempts have been made to understand its role as both an intraspecies and interspecies signal.

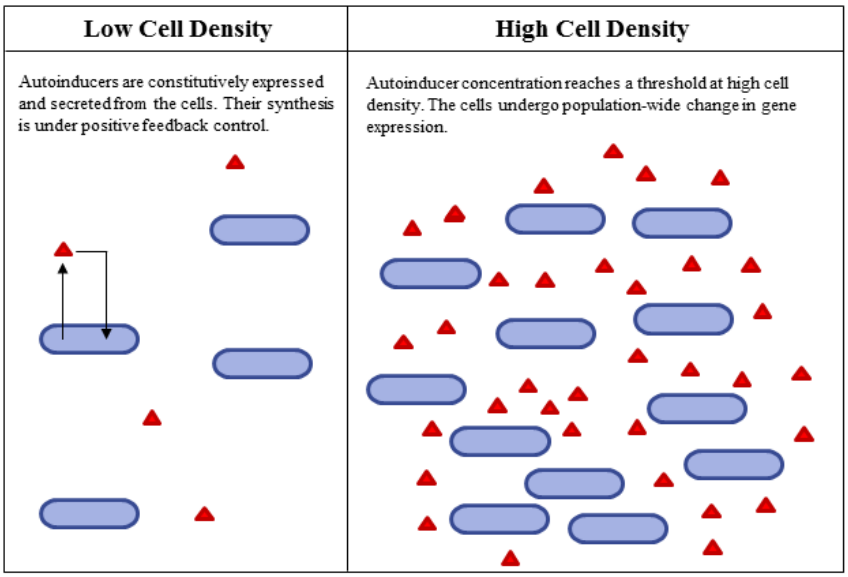

Figure 1: Quorum sensing using autoinducers. Cells (gray) use autoinducers (red triangles) to detect the surrounding population density. At low cell densities, autoinducers are present at low concentrations. At high cell densities, autoinducer concentration reaches a threshold and induces expression of genes involved in population density-dependent collective behaviors.

I.3 Autoinducer 2: An Overview

AI-2 is a five carbon furanone synthesized by the enzyme LuxS as part of the *S*-adenosyl methionine (SAM) degradation pathway (Figure 2). This pathway is present in Gram-positive and Gram-negative bacteria, including *Streptococcus gordonii*, *Sreptocococcus oralis*, *Bifidobacterium breve*, *Lactobacillus acidophilus*, *Vibrio cholerae*, *E. coli* (including EHEC), *Helicobacter pylori* and *Salmonella enterica* serovar Typhimurium. Homologs of *luxS* have been identified in several sequenced bacterial genomes (17, 18).

Unlike other autoinducers, AI-2 is not one entity but rather a family of chemical species that exist in equilibrium (Figure 3) (20, 21). The two cyclized forms, *R*-THMF and *S*-THMF, are sensed by different receptors in different species. The *R*-THMF form is bound by the periplasmic binding protein LsrB in *S. enterica*, *E. coli*, *Yersinia pestis*, and *Sinorhizobium meliloti* (20, 22-24), whereas the borated form of *S*-THMF is bound by LuxP in several Vibrionales, including *V. harveyi* (25).

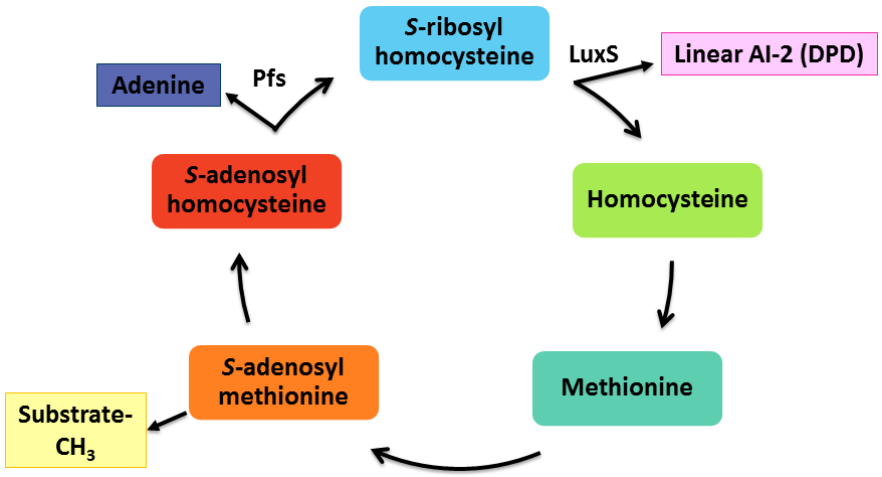

Figure 2: AI-2 is synthesized as part of the SAM pathway. Release of the methyl group from SAM results in the formation *S*-adenosylhomocysteine (SAH). SAH is toxic and is immediately converted to *S*-ribosylhomocysteine (SRH) and adenine by the enzyme Pfs. The AI-2 synthase, LuxS, then breaks down SRH to form AI-2 (linear form) and homocysteine. Homocysteine is used to recycle methionine which is converted to SAM. AI-2 is exported from the cell.

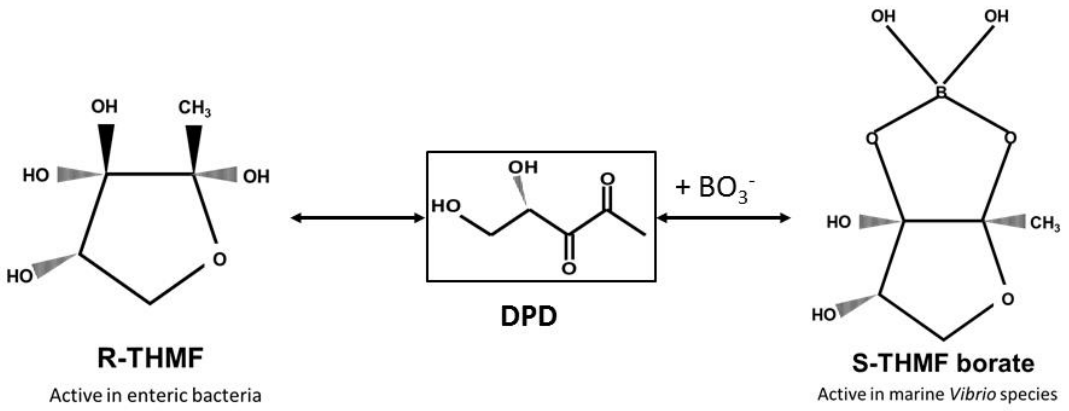

Figure 3: The three chemical forms of AI-2. The linear LuxS product of the SAM pathway, S-4,5-dihydroxy-2,3-pentandione (DPD, in center), spontaneously hydrates and cyclizes to form S-2-methyl-2,3,3,4-tetrahydroxytetrahydrofuran (S-THMF) and R-2-methyl-2,3,3,4-tetrahydroxytetra-hydrofuran (R-THMF, on left). When borate is present in the environment, S-THMF binds it to form S-THMF borate (on right). These three forms of AI-2 exist in equilibrium with each other.

Several studies have attempted to understand the QS-dependent signaling role of AI-2 in regulating different functions in their organism of interest by knocking out the *luxS* gene and then identifying changes in gene expression and group behaviors (reviewed in ref. (26)). The absence of LuxS, and therefore AI-2 signaling, has been shown to influence several behaviors, including motility, chemotaxis and biofilm formation in *H. pylori* (27-29), virulence and biofilm formation in *Vibrio cholerae* (30, 31), biofilm formation in *Bacillus cereus* (32), biofilm formation in *Staphylococcus aureus* (33), motility and HeLa cell attachment in EHEC (9) and resistance to antibiotics in *Streptococcus anginosus* and *Streptococcus intermedius* (34, 35). The absence of LuxS leads to metabolic defects in several organisms, and it is therefore often difficult to

establish whether the observed phenotypic changes are due to signaling defects, metabolic defects, or both (26, 36, 37). Some studies have been able to identify AI-2 signaling-dependent defects by supplementing the cells with synthetic AI-2. For example, Shao *et al* showed that biofilm growth of an *Aggregatibacter actinomycetemcomitans luxS* mutant can be restored by adding AI-2 to the growth medium (38). A few studies have focused on understanding the interspecies signaling role of AI-2. Xavier and Bassler (39) made the first attempt by co-culturing *V. harveyi* and *E. coli*. Their studies found that *V. harveyi* responds to AI-2 produced by *E. coli* by inducing bioluminescence, and AI-2 made by *V. harveyi* induces the AI-2 regulated *lsrACDBFG* operon in *E. coli*. They also found that accumulation of *E .coli* AI-2 leads to induction of *V. cholerae hapA*, a haemagglutin protease that facilitates detachment from the intestinal mucosa (40). Detachment and shedding are important for the spread of cholera, suggesting that the availability of AI-2 within the mammalian gut could influence the pathogenecity of *V. cholerae*. In the oral cavity, interspecies AI-2 signaling has been shown to regulate mutualistic biofilm formation. The human oral commensal bacterium *Actinomyces naeslundii* lacks *luxS* and only forms biofilms in the presence of AI-2 secreted by *Streptococcus oralis* or synthetically supplied AI-2, providing further evidence of AI-2 as an interspecies signal (41). *Porphyromonas gingivalis* is a periodontal pathogen that typically forms biofilms with *Streptococcus gordonii*. McNab *et al* showed that biofilm formation did not occur if both organisms lacked *luxS*. However, the presence of *luxS* in one of the species was sufficient to restore mixed-

species biofilm formation, providing another example of an interspecies signaling role for AI-2 (42, 43).

I.4 Autoinducer-2 in *E. coli*: A Different Paradigm

In *E. coli*, AI-2 is produced during mid-exponential phase and begins to accumulate extracellularly during late-exponential phase. Unlike other autoinducers that accumulate extracellularly at high cell densities, AI-2 is rapidly removed from the medium during stationary phase (44). Furthermore, AI-2 has not been shown to bind directly to cell surface receptors to induce signal transduction pathways that mediate changes in gene expression in *E. coli*. Instead, *E. coli* has a system dedicated to the uptake and processing of AI-2 called the LuxS regulated (Lsr) system (Figure 4). The Lsr system consists of two divergently transcribed operons, *lsrRK* and *lsrACDBFG*. The *lsrACDBFG* operon contains genes for AI-2 uptake and degradation, whereas *lsrRK* contains regulatory proteins. LsrB binds periplasmic AI-2 and this complex interacts with the ATP-binding cassette (ABC) transporter LsrACD to internalize AI-2. LsrK phosphorylates internalized AI-2 (44). LsrF and LsrG degrade phosphorylated AI-2 (P-AI-2). LsrR represses both the operons in the absence of phosphorylated AI-2 (P-AI-2). The presence of P-AI-2 leads to the de-repression of both the operons and the consequent synthesis of uptake, processing, and degradation components (45, 46). Interfering with AI-2 synthesis or the Lsr system leads to defects in phenotypes such as motility and biofilm formation and architecture (7, 8, 47, 48), suggesting that AI-2 mediates quorum sensing-dependent behaviors in this organism.

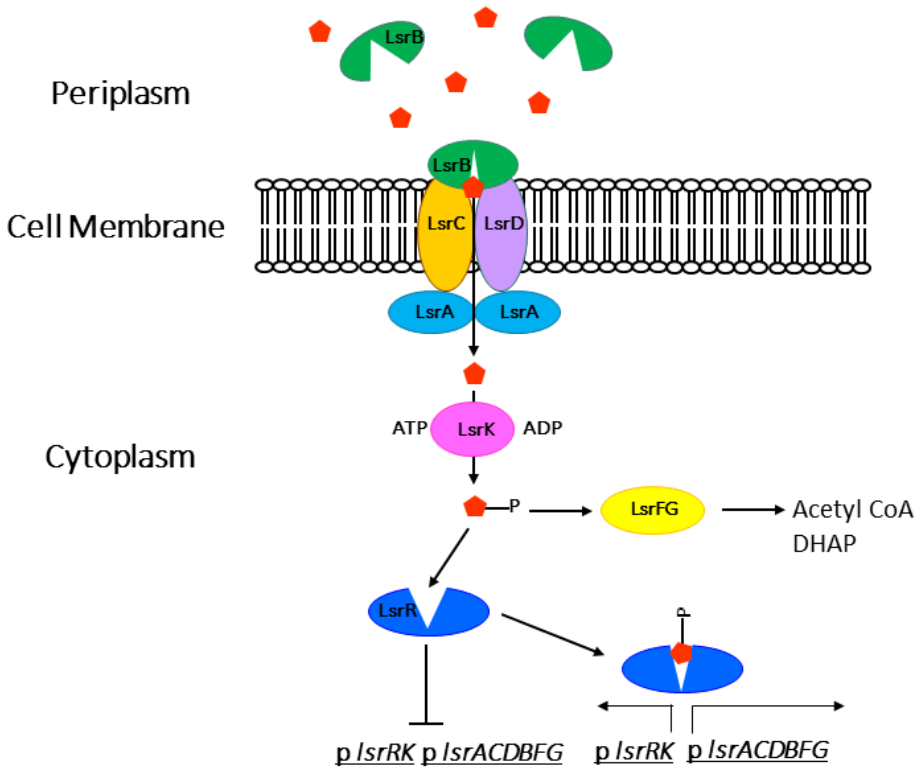

Figure 4: Uptake, processing, and degradation of AI-2 in *E. coli*. AI-2 (red pentagons) diffuses into the periplasm and is bound by the binding protein LsrB. LsrB bound AI-2 interacts with the ABC transporter LsrACD to transport AI-2 into the cell. Internalized cytoplasmic AI-2 is phosphorylated by LsrK. P-AI-2 binds to LsrR to relieve repression of the *lsrRK* and *lsrACDBFG* operons. AI-2-P is simultaneously isomerized by LsrG to make 3-hydroxy-2,4-pentanedione-5-phosphate (P-HPD), which exists in equilibrium with its hydrated form 3,4,4-trihydroxy-2-pentanone-5-phosphate (P-TPO) (1). P-HPD is then broken down into acetyl-CoA and dihydroxyacetone phosphate (DHAP) by LsrF (2).

I.5 The Chemotaxis System in *E. coli*

E. coli is a Gram-negative bacillus belonging to the *Enterobacteriaceae* family. The cells are about 2-4 μm long and 0.5-1 μm in diameter. Thin, left-handed helical flagella protrude from seemingly random spots on the cell surface. Flagellar rotation propels the bacteria through liquid or semi-solid media, allowing them to swim as fast as 30 μm/s.

In a homogenous medium, an *E. coli* cell swims in a random pattern that is characterized by alternating runs and tumbles (Figure 5A). A run, an interval of smooth swimming that occurs when the flagellar filaments bundle together and rotate in the counterclockwise (CCW) direction, typically lasts for several seconds. Clockwise (CW) rotation of the filaments disrupts the flagellar bundle, causing the bacteria to tumble and reorient in a random direction. A typical tumble lasts for less a fraction of a second.

Natural environments are rarely homogenous, and bacteria encounter gradients of chemical ligands (called chemoeffectors) while swimming through them. They are capable of sensing spatiotemporal changes in the concentrations of chemoeffectors, and this ability allows cells to bias their movement up or down concentrations gradients of attractant and repellent molecules, respectively (49). This behavior is called chemotaxis (Figure 5B). Runs are longer when moving up an attractant gradient or down a repellent gradient.

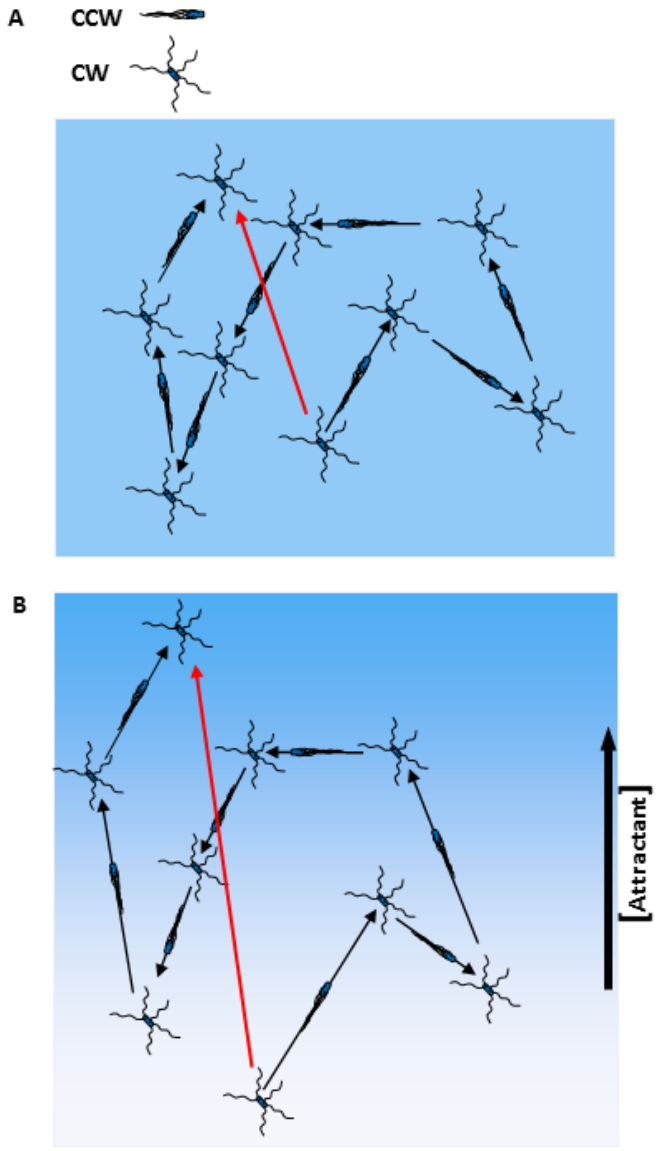

Figure 5: Movement of an *E. coli* cell in three-dimensional space. A) Movement in a homogenous medium (uniform blue background) is random and is characterized by alternating runs (CCW) and tumbles (CW). B) Movement becomes biased in the presence of a chemoeffector gradient. The black arrow points from low to high attractant concentration. The red arrows represents the net displacement of the cell.

The well-studied chemotaxis signaling cascade that controls flagellar rotation in *E. coli* is shown in Figure 6. Attractant or repellent ligands bind to transmembrane methyl accepting chemotaxis proteins (MCP) in the periplasm. MCPs transduce the signal from ligand binding to a cytoplasmic histidine protein kinase CheA. Autophosphorylated CheA in turn transfers the phosphoryl group to two response regulators, CheY and CheB. Alternating runs and tumbles occur because of a finely tuned balance between CheY and CheY-P levels. The methylation state of the receptor allows cells to adapt to the current chemoeffector concentration, which permits sensing spatiotemporal changes in concentrations. CheB-P, a methylesterase, removes methyl groups from the receptor that are added by CheR, a methyltransferase. The interplay between these enzymes controls the methylation state of the receptor.

The chemosensory system is located at the cell poles, being larger at the old cell pole, and it is highly organized (3, 50, 51). This high level of organization results from the clustering of individual MCP homodimers. MCPs of the same or different types cluster together to form stable trimers of dimers in the presence of CheA and the adaptor protein CheW. These organized clusters contribute to the sensitivity of the chemotaxis system by allowing signal amplification upon binding of a ligand (3).

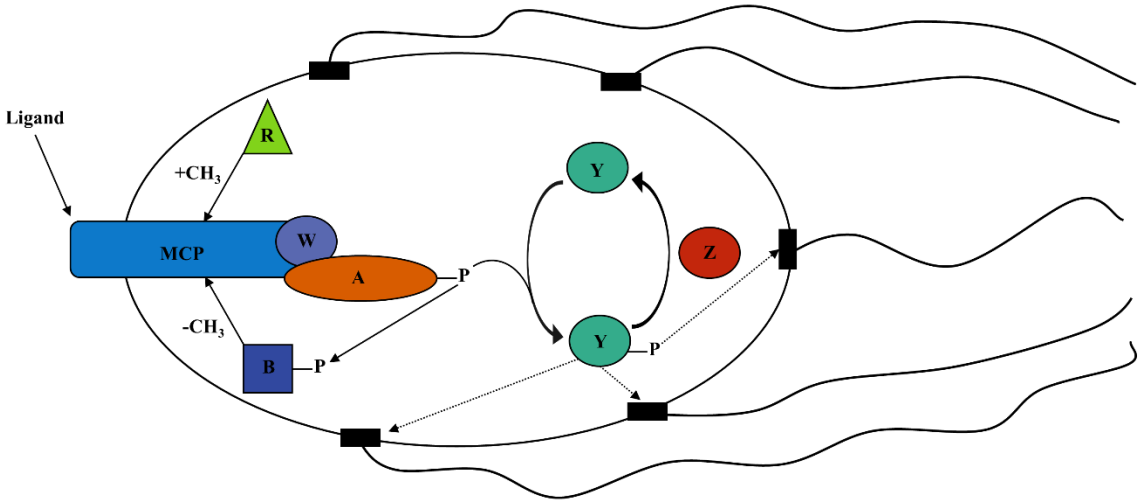

Figure 6: Chemotaxis signaling cascade in *E. coli*. Changes in ligand (attractant or repellent) concentrations are sensed by MCPs, the adaptor protein CheW (W), and the histidine kinase CheA (A). Binding of an attractant inhibits CheA autophosphorylation, whereas binding of a repellent enhances it. Autophosphorylated CheA (A-P) transfers a phosphoryl group to CheY (Y). Phosphorylated CheY (Y-P) diffuses to the flagellar motor (black box) and binds to the motor switch protein FliM. This results in a change in the rotational direction of the motor from CCW to CW. When the flagella rotate CW, the flagellar bundle is disrupted, and the cells tumble. The enzyme CheZ (Z) is a phosphatase that dephosphorylates CheY-P and controls the frequency of runs and tumbles by controlling the ratio of CheY:CheY-P. Adaptation of the system to chemoeffector concentrations is mediated by two enzymes: the methyltransferase CheR (R) and the methylesterase CheB (B). CheR and CheB add or remove, respectively, methyl groups at specific glutamyl residues on each MCP monomer. The ratio of methyl groups determines the sensitivity of the receptor to chemoeffectors. Adapted from ref. (3).

I.6 Chemotaxis toward Signals in *E. coli*

Directed movement of bacteria in response to environmental stimuli such as nutrients and toxins, temperature, pH, osmolarity, oxygen, reduction potential and light have been

explored by many researchers since the tactic behavior of bacteria was first discovered (51, 52). Recently, a few groups have initiated investigations using pathogenic bacteria such as *H. pylori*, *Salmonella enterica* serovar Typhimurium and EHEC to understand how chemical signals produced by other bacteria or the host contribute to niche recognition, attachment, proliferation and, ultimately, virulence in these organisms (9, 11, 29, 53-56).

E. coli is primarily found in the intestines of warm blooded mammals as well as some birds, reptiles and fish. It is also found in sewage, and cells can make their way into food and water if these are contaminated with sewage (5). While moving through the GI tract, *E. coli* encounters an enormous array of molecules, many of which serve as chemoeffectors sensed by the chemotaxis system. These molecules originate from multiple sources: they can be nutrients derived from the diet, such as sugars and amino acids, or signal molecules released by other microbial inhabitants, such as AI-2, acyl homoserine lactones, indole, or signal molecules released by the host, such as the neurotransmitters norepinephrine and serotonin. It has been speculated that the integration of responses to all these molecules influences the behavior and ultimate localization of *E. coli* within the gut.

The interspecies signal AI-2 is a five carbon furanone synthesized by the enzyme LuxS as part of the SAM pathway. The SAM pathway and homologs of *luxS* are present in several Gram-positive and Gram-negative bacteria, including several mammalian commensals and pathogens. Bansal *et al.* predicted that this ubiquitous signal could

potentially affect the virulence and infection ability of EHEC within the GI tract by influencing virulence phenotypes such as motility, chemotaxis and attachment to epithelial cells (9). Their study was the first to identify that AI-2 is sensed as a chemoattractant. They also found that AI-2 increases EHEC motility and adherence to HeLa cells. They concluded that, as AI-2 leads to an increase in virulence phenotypes that contribute to colonization, it is likely that the presence of AI-2 within the GI tract enhances EHEC virulence.

In *E. coli*, ligands are sensed directly by the periplasmic domains of transmembrane methyl-accepting chemotaxis proteins (MCPs) or indirectly when they bind to periplasmic binding proteins that then interact with the MCP. *E. coli* has four transmembrane MCPs: the *L*-serine receptor Tsr, the aspartate/maltose receptor Tar (57), the galactose/ribose receptor Trg (58, 59), and the dipeptide/pyrimidine receptor Tap (60, 61). The fifth chemoreceptor, Aer, cannot be methylated and is involved in mediating aerotaxis by monitoring redox changes in the electron transport chain (62). Tar, Tsr and Aer are well preserved with a high degree of sequence homology in both commensal and pathogenic *E. coli*, whereas Trg and Tap are absent from a majority of pathogens (63, 64).

Hegde *et al* used non-pathogenic *E. coli* strain RP437 as a model to determine which of the five receptors is involved in chemosensing AI-2. Their study showed that chemotaxis toward AI-2 is mediated by Tsr. Moreover, AI-2 is sensed indirectly; it must first be recognized by the AI-2 binding protein LsrB, which in its ligand-bound form

docks onto Tsr. This report was the first to identify a periplasmic binding protein that interacts with Tsr. That study raised several questions related to the molecular mechanism involved in sensing an AI-2 gradient and to the ecological benefit of doing so. Both of those questions are addressed in this study.

CHAPTER II

INVESTIGATING THE ROLE OF AI-2 CHEMOTAXIS IN BIOFILM FORMATION

II.1 Overview

E. coli produces and secretes the quorum-sensing (QS) signal AI-2 during active growth. In shaking cultures, AI-2 accumulates extracellularly during late exponential phase and is then rapidly imported and degraded. AI-2 signaling resulting from internalization regulates patterns of gene expression that promote biofilm development. *E. coli* can also migrate up an extracellular gradient of AI-2, which requires the periplasmic binding protein LsrB and the *L*-serine chemoreceptor Tsr. As AI-2 influences both biofilm formation and chemotaxis, I undertook this study to determine whether chemotaxis to AI-2 contributes to biofilm formation. Using the crystal violet staining assay to quantify surface-attached biofilm biomass, I found that, under static conditions, GFP-tagged *E. coli* RP437 cells (WT) cells adhere to a surface more strongly than cells lacking components required for AI-2 chemotaxis or AI-2 production. Decreased attachment of the knockout strains is possibly influenced by interactions occurring during the initial stages of biofilm development. My observations show that strains lacking LsrB and Tsr form self-aggregates and microcolonies on a surface at a slower rate than WT. The behavior of these knockouts resembles that of Δ*luxS* cells that do not produce AI-2, suggesting that the presence of AI-2 and the ability to chemo-sense it are required to form cellular aggregates. Strains defective strains in AI-2 uptake and processing respond like WT cells to an external AI-2 gradient, but they are defective in both initial

aggregation and biofilm formation. These data suggest that chemotaxis to external AI-2 is insufficient to induce the full range of density-dependent behaviors; an intact AI-2 uptake and processing system is required for optimal aggregation and biofilm formation.

II.2 Introduction

Bacteria rarely exist as individual cells in natural environments. They form complex surface-attached communities, called biofilms that are encased in an extracellular matrix composed of polysaccharides, proteins, and nucleic acids. Living in a biofilm allows cells to capture and share nutrients more effectively and also remain protected against environmental challenges such as exposure to antimicrobial agents and attack by the host immune system (65-70). Biofilm development on a surface begins when planktonic cells sense and reversibly attach to the surface by incorporating information obtained from several mechanical and chemical cues (71-77). Reversibly attached cells commit to the surface after sensing the local environment (78, 79). Irreversible attachment onto the surface in facilitated by turning off the expression of genes that promote a planktonic lifestyle. In Gram-negative bacteria, for example, flagella and pili expression is turned off and expression of exopolysaccharides (EPS) and adhesins that promote irreversible attachment is turned on (80). The pattern of gene expression changes in response to signals regulated, at least in part, by quorum-sensing molecules. These induce the initiation and maturation of biofilms, which can be very complex both in species composition and in three-dimensional architecture (81, 82).

Reversible attachment of motile bacteria to a surface is facilitated by flagellar rotation. Active motility allows cells to overcome the repulsive electrostatic and hydrodynamic forces associated with surfaces and facilitates the transition from life in the bulk medium to life on the surface (47, 66, 80, 83-85). Flagellar rotation has also been implicated in triggering cell-cell interactions by altering hydrodynamic conditions surrounding cells. Cell-cell interactions may enhance surface attachment via the formation of aggregates with high enough local population densities that promote the quorum-sensing dependent behavior and patterns of gene expression required for biofilm formation (86). Chemotaxis regulates the migration of planktonic cells by causing changes in the direction of flagellar (51, 87). It is possible that changing patterns of flagellar rotation may promote interactions among cells and between cells and the surface that are important during the initial stages of biofilm development (86). Some studies suggest that cells trap ions and small molecules in a thin layer of fluid between the cell body and the surface once they attach to the surface. This leads to the formation of a microenvironment that is unique to the attached cell (88). Chemical gradients emanating from such microenvironments may serve to attract planktonic cells.

E. coli secretes the interspecies signaling molecule AI-2 during active growth. AI-2 is synthesized by the enzyme LuxS as part of the *S*-adenosyl methionine (SAM) pathway that donates methyl groups to various substrates for carrying out essential functions such as DNA and protein methylation. AI-2 has been shown to regulate collective behaviors such as attachment, virulence, and biofilm formation in *E. coli* (7, 8, 48, 53). It is also a

chemoattractant that is sensed by the *L*-serine chemoreceptor Tsr (11). In this study, I asked whether AI-2-producing surface-attached cells attract planktonic cells and whether AI-2 chemotaxis contributes to the formation of self-aggregates. As aggregation is a precursor to biofilm formation, I also asked if chemotaxis to AI-2 affects biofilm formation on a surface.

Aggregation and attachment are essential factors in establishment of infections caused by pathogenic *E. coli* such as EHEC (89). The resulting biofilm formation is key for the persistence of chronic inflammatory conditions within the gut by pathobionts such as Adherent Invasive *E. coli* (AIEC) (90). Understanding the role of AI-2 chemotaxis in the colonization of the gut epithelium by pathogenic *E. coli* should contribute to the development of novel methods to combat these organisms by interfering with their ability to form biofilms.

II.3 Materials and Methods

Bacterial strains, chemicals, and growth media

E. coli RP437, the lab strain that has been widely used to study chemotaxis (91), transformed with the GFP-expressing (*gfp*mut3*) plasmid pCM18 (provides resistance to erythromycin) (92) is the wild-type strain used in this study (referred to as WT). All other strains used in this study are listed in Table 1. Gene deletions were made using P1 transduction (93, 94) and kanamycin cassettes were eliminated using FLP recombination (95, 96). Primers used to verify gene deletions are listed in Table 2. Overnight cultures were either grown in tryptone broth medium (TB; 10 g/L tryptone, 10 g/L NaCl) or Luria Bertani medium (LB; 10 g/L tryptone, 10 g/L NaCl, 5 g/L yeast extract) at 30°C, 250 rpm. All strains were grown in TB medium for OD_{600nm} growth measurements at 30°C, 250 rpm. AB minimal medium supplemented with 0.5% casamino acids (BD Biosciences, USA) and 2.5 mg/mL thiamine hydrochloride (Alfa Aesar, USA) (ABTCAA) (97) was used for observing aggregation and in the crystal violet biofilm formation assay. Overnight culture media contained 100 µg/mL erythromycin (VWR, USA) to maintain pCM18. No antibiotics were added to the medium for the other assays.

Observation of self-aggregation

To observe aggregation and determine whether there were differences in aggregations among the strains, I introduced cells into non-coated 96 well polystyrene plates (Costar; Corning, USA) or non-coated cover glass wells (Nunc ® Lab-Tek™ chambered cover

glasses, 8 chambers, VWR, USA) and then obtained two dimensional images using fluorescence microscopy (Carl Zeiss Axiovert 200M inverted microscope; 20x objective; total magnification = 200x). All strains were grown to saturation (16 h) in LB with 100 µg/mL erythromycin at 30°C with shaking at 250 rpm. The cultures were diluted to 10^7 cells/mL in ABTCAA medium. 200µL of the diluted culture was introduced into each well. The plates or 8-chambered wells were placed in a humidified chamber at 30°C or 37°C and imaged at the specified time points (one plate per time point).

Table 1: Strains used in this study.

Strain name in text	Relevant genotype or phenotype[a]	Reference
Δ*luxS*	*E. coli* RP437Δ*luxS*/pCM18 Erm^R Stm^R	This study
Δ*lsrB*	*E. coli* RP437 Δ*lsrB*/pCM18 Erm^R Stm^R	This study
Δ*tsr*	*E. coli* RP437Δ*tsr*/pCM18 Erm^R Stm^R	(11)
Δ*lsrC*	*E. coli* RP437Δ*lsrC*/pCM18 Erm^R Stm^R	This study
Δ*lsrR*	*E. coli* RP437Δ*lsrR*/pCM18 Erm^R Stm^R	This study
Δ*lsrK*	*E. coli* RP437Δ*lsrK*/pCM18 Erm^R Stm^R	This study
TL-26	*V. harveyi* Δ*luxN* Δ*luxS* Δ*cqsS*	(104)

[a] Stm – streptomycin, Erm – erythromycin

Table 2: Primers used for PCR verification of Km^R insertion mutants.

Primer Name	Sequence (5'- 3')	Source
K1	CAGTCATAGCCGAATAGCCT	(95)
lsrC_F	CAGCATCGCCGCACAAAATG	This study[a]
lsrC_R	GCAGATAAAGTCACTGGTGCTGAAC	This study[b]
lsrR_F	GCTCGTAGAGTCAAACTGTGGT	This study[b]
lsrR_R	ATCTCAGCCCGAATACTTCCG	This study[b]
lsrK_F	GATCAGGACACAGCAGCGG	This study[b]
lsrR_R	ACGATGAATCTGCAAGCTGGCTT	This study[b]

[a] F = forward or upstream primer [b] R stands for reverse or downstream primer

Image processing

Cells of the same biological replicate were imaged in different plates at the specified time points. I used a constant exposure time (between 100-300 ms) to avoid overexposing cells or introducing artifacts. All images were adjusted for sharpness, brightness, and contrast using the 'auto adjust colors' option in IrfanView (Irfan Skiljan, http://www.irfanview.com/). To clearly show the cellular aggregates the initial images, I split each image (1388 x 1040 pixels) by three rows x three columns into 9 total images (462 x 346 pixels) using the montage to stack option in ImageJ (98).

Quantitative analysis of aggregates in images

I used a simple code written in Matlab R2016b (Mathworks, USA) to quantify the differences in aggregation. The analysis consisted of the following steps: (i) thresholding of the raw grayscale images using the Otsu filtering method to generate binary images where high intensity pixels are set to 1, white, and low intensity pixels are set to 0, black; (ii) objects were then constructed by grouping each white pixel from each threshold image into an object (each object is composed of a set of connected white pixels); (iii) objects above a certain size (in number of pixels) for each image were identified; and the aggregate number of pixels in those objects was summed and divided by the total number of pixels with a threshold of 1 in the corresponding image. This ratio was plotted for each strain and allowed me to compare aggregation among the strains.

Quantification of attached biomass using crystal violet

Polystyrene plates have been extensively used to study biofilm development, which is the reason I chose to study aggregation and biofilm formation on this surface (84, 97, 99). Indirect determination of biomass attached to the wells of the polystyrene plate was determined using the well-established crystal violet assay. Crystal violet stains extracellular matrix polymers and cells (99, 100). Briefly, strains were grown to saturation (16 h) in TB with 100 µg/mL erythromycin at 30°C with shaking at 250 rpm. The cultures were diluted to 10^7 cells/mL in ABTCAA medium. 200µL of the diluted culture was introduced into each well. The plates were placed in a humidified chamber at

30°C or 37°C. At the specified time point, the density of suspended cells was measured by reading OD_{600nm} using a microplate reader (Molecular devices, USA). Unattached cells were discarded from the wells which were then rinsed once with distilled (DI) water to remove any remaining loosely attached cells. The plates were air dried overnight or at 37°C for one hour. 250 µL of 0.1% crystal violet (CV) was introduced into each well and the plate was incubated for 15 minutes at room temperature. The CV was discarded and the wells were rinsed thrice with DI water. Excess water from the wells was removed by dabbing the plate on blotting paper. The plates were air dried overnight or at 37°C for one hour. 250 µL of 33% acetic acid was introduced into each well. The solubilized CV from the stained cells was transferred to a new plate and the absorbance was read at 590 nm using a microplate reader (Molecular devices, USA).

Vibrio harveyi *bioluminescence assay*

V. harveyi TL-26 was used to detect AI-2 accumulation in biofilm culture fluids as previously described (101). Briefly, 100 µL of biofilm culture fluid was collected at the desired time point centrifuged at 16,100 x *g* for 10 min at 4°C. 10% of the cell-free supernatant was added to 90% TL-26 culture (1:5000 in AB medium) in an opaque white 96-well plate (Greiner Bio-One, USA) and incubated at 30°C for 4 h. Luminescence from each well was read using the Mithras LB940 Multimode Microplate reader (Berthold, USA). Luminescence output from the reader is expressed as Relative Light Units (RLU) per second. Luminescence output of the control wells i.e. ABTCAA medium only is negligible at this time point. The luminescence of the samples is

represented as fold induction in bioluminescence which is obtained by background normalizing the sample RLU.

Determination of chemotaxis response using capillary assays

Capillary assays were carried out as previously described (102) with the following modifications for preparing cells before introducing them into chemotaxis chambers. Cells were centrifuged at 600 x *g* for 10 min, followed by gentle resuspension in a volume of chemotaxis buffer (CB, 1X phosphate-buffered saline, 100 µM EDTA, 1 µM L-methionine, and 10 mM lactic acid, pH 7.4) such that the final OD_{600nm} = ~0.5. The tubes were then placed on a low-speed tube roller at 30°C for 15 min before being introduced into the chemotaxis chambers. The number of cells accumulated in the capillary was determined by subtracting the accumulation of cells in CB from the accumulation of cells in the presence of the attractant.

Generation of growth curves

All strains were grown in TB medium or ABTCAA medium with swirling at 250 rpm for aeration, and the optical density (OD_{600nm}) of the culture was measured at the specified time points.

Swim plate assay for observing chemotaxis and motility

All strains were grown in LB medium with 100 µg/mL erythromycin for 16 h at 30°C, 250 rpm. 2.5 µL of each culture was placed on the surface of freshly poured 0.3% TB

agar plates. Plates were incubated at 30°C for 16 h, at which time the diameter of the swimming zone (cm) was measured.

Congo red assay for detection of curli production

Curli production was assessed by streaking strains on YESCA congo red plates (10 g/L casamino acids, 1 g/L yeast extract, 20 g/L agar, 50 µg/mL congo red (103). Plates were incubated at 30°C or 37°C for maximum time of 72 h. Colony color was checked every 24 h.

II. 4 Results

Bacteria exist within surface-attached, matrix-enclosed communities called biofilms in almost all natural environments. The process of formation and maintenance of biofilms is extremely complex and entails social interactions between different microbes as well as between the organisms and the environment (67). Biofilm development has been extensively researched since biofilms were first identified by Anton Von Leeuwenhoek in plaque from his teeth in the 17th century. Under lab conditions, biofilms are studied using various techniques, including confocal laser scanning microscopy (CLSM), biofilm-staining assays, and metabolic assays. The technique used determines the information obtained about a specific aspect of biofilm development. For example, CLSM is widely used to study thick, three-dimensional biofilms as it provides insight into the spatial distribution of cells and matrix components within the biofilm (105-107).

In this study, I used the crystal violet assay to evaluate biofilm formation as a measure of surface attached biomass.

E. coli resides primarily in the intestines of warm-blooded mammals that maintain their temperature around 37°C (4). Its secondary habitat is outside the host, where it is found in soil, sewage, water bodies and contaminated food sources (108, 109). *E. coli* has evolved several mechanisms to modulate its behavior based on environmental conditions (110). Hence, I performed all the experiments in this study at both 30°C and 37°C which are representative of *ex vivo* and *in vivo* temperatures respectively.

Biofilm formation on an abiotic surface

I quantified biofilm formation of Δ*lsrB* and Δ*tsr* strains and compared it to that of WT and Δ*luxS* strains to determine whether components required for AI-2 chemotaxis affect biofilm formation. Figures 7A and 7B show that there is more biomass attached to the polystyrene wells with the WT strains than with the Δ*lsrB*, Δ*tsr* and Δ*luxS* strains after 24 hours of incubation at both 30°C and 37°C. These data suggest that knocking out AI-2 production or the components required for sensing AI-2 as an attractant decrease adherence to an abiotic surface. More biomass attached to the polystyrene wells at 37°C compared to 30°C with all strains. This could, in part, be due to a decrease in the motility of *E. coli* RP437 cells at 37°C.

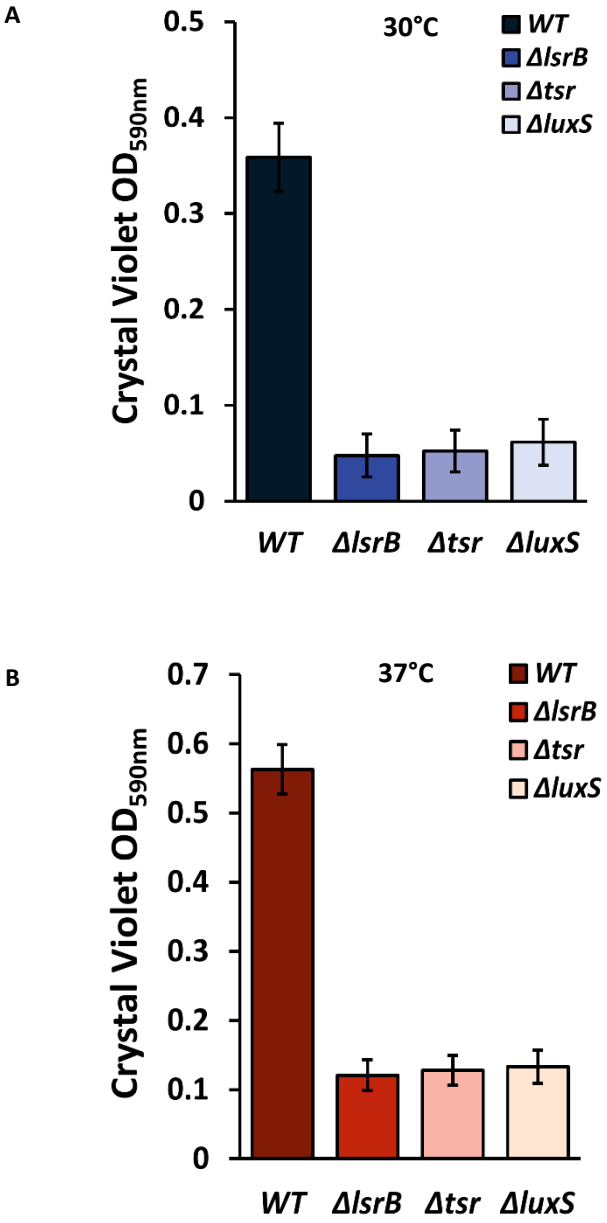

Figure 7: Quantification of attached biofilm biomass using the crystal violet assay. Cells were grown in 96-well polystyrene plates as described in Methods and were incubated for 16 h or 24 h at 30°C (A) or 37°C (B). Data shown are averages of five replicate wells each for six biological replicates. Error bars represent the standard error of the mean of the replicates.

Flagellar rotation promotes surface sensing and attachment during initial stages of biofilm development. Chemotaxis toward or away from molecules also affects the rotation of flagella. I hypothesized that the defect seen in biofilm formation on polystyrene plates could be mediated by AI-2 chemotaxis-dependent interactions during the initial stages of attachment and growth on a surface.

Self-aggregation on an abiotic surface

To test this hypothesis, I observed the behavior of GFP-tagged cells on the bottom surface of polystyrene wells using fluorescence microscopy and measured extracellular AI-2 accumulation using the *V. harveyi* bioluminescence assay (111). As chemotaxis to AI-2 requires the periplasmic LsrB binding protein and the Tsr chemoreceptor, I compared the behavior of WT with that of isogenic strains lacking these key components.

I first ensured that knocking out *lsrB, tsr*, and *luxS* did not affect growth rate or overall chemotaxis and motility of the strains. As seen in Figure 8A, the growth rate of all the strains is similar. In ABTCAA medium, all four strains also grow similarly with shaking for aeration, but they saturate at OD_{600nm} = 0.5 (data not shown). The cells of all four strains appeared vigorously motile when observed under the microscope, and the formation of chemotaxis rings in 0.3% TB agar was comparable for WT, Δ*lsrB*, and Δ*luxS* (Figure 8B). The Δ*tsr* mutant cannot sense a serine gradient, and hence it lacks the outer chemotaxis ring formed by the other strains and forms a colony of lower diameter.

Even the inner aspartate ring is smaller because of the altered run-tumble frequency of the Δ*tsr* mutant relative to the *tsr*$^+$ strains.

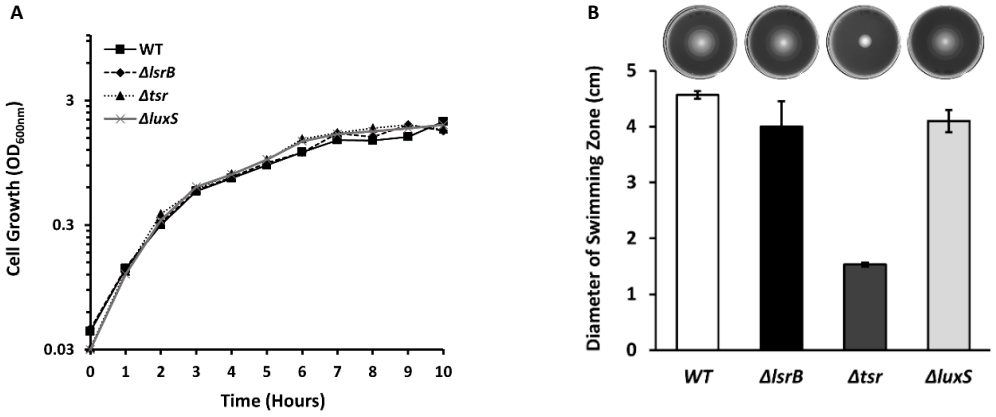

Figure 8: Growth and motility of WT and isogenic Δ*lsrB*, Δ*tsr*, and Δ*luxS* deletion mutants. A) Growth of all strains in TB medium with aeration as a function of optical density (OD600nm). Data from one independent replicate are shown. B) Histogram depicting the diameter of the swimming zone (cm). Data shown are averages of four independent replicates. Error bars represent the standard error of the mean of the replicates. A sample image of a swim plate for each strain is shown above its bar.

To observe the behavior of cells on a surface, I seeded a low density (10^7 cells/mL) of cells from a saturated ABTCAA culture into the wells of 96-well polystyrene plates, incubated them in a humidified chamber, and imaged cells on the bottom surface every 2-4 h. Cells were not in aggregates at the time of seeding, as can be seen in Figure 9.

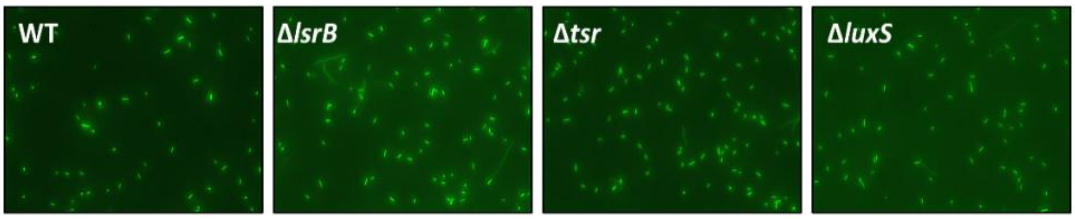

Figure 9: GFP-tagged WT, Δ*lsrB,* Δ*tsr,* and Δ*luxS* at the time of seeding. All strains were grown and diluted in ABTCAA medium as described in methods. 50 µL of the culture was placed on a 22x22 mm coverslip. Cells were imaged using the 63x objective.

Within 2 h of incubation, self-aggregates, which appear as multiple cells close together on the surface and on top of each other, were seen with WT cells Self-aggregates were small and infrequent in the Δ*lsrB*, Δ*tsr*, and Δ*luxS* strains (Figure 10).

Quantitative analysis of the acquired images was performed using 50 pixels as the threshold aggregate size. Figure 11 shows examples of threshold images containing aggregates larger than 50 pixels outlined in red. The images in Figure 11 correspond to those in Figure 10. The images show that self-aggregates are not totally absent in Δ*lsrB*, Δ*tsr*, Δ*luxS*. The aggregates, are however, smaller in size. A majority of these aggregates are likely to be dividing cells that tend to be close together. A few of the aggregates have a three dimensional appearance. A histogram depicting the fraction of pixels in aggregates in the strains is shown in Figure 12.

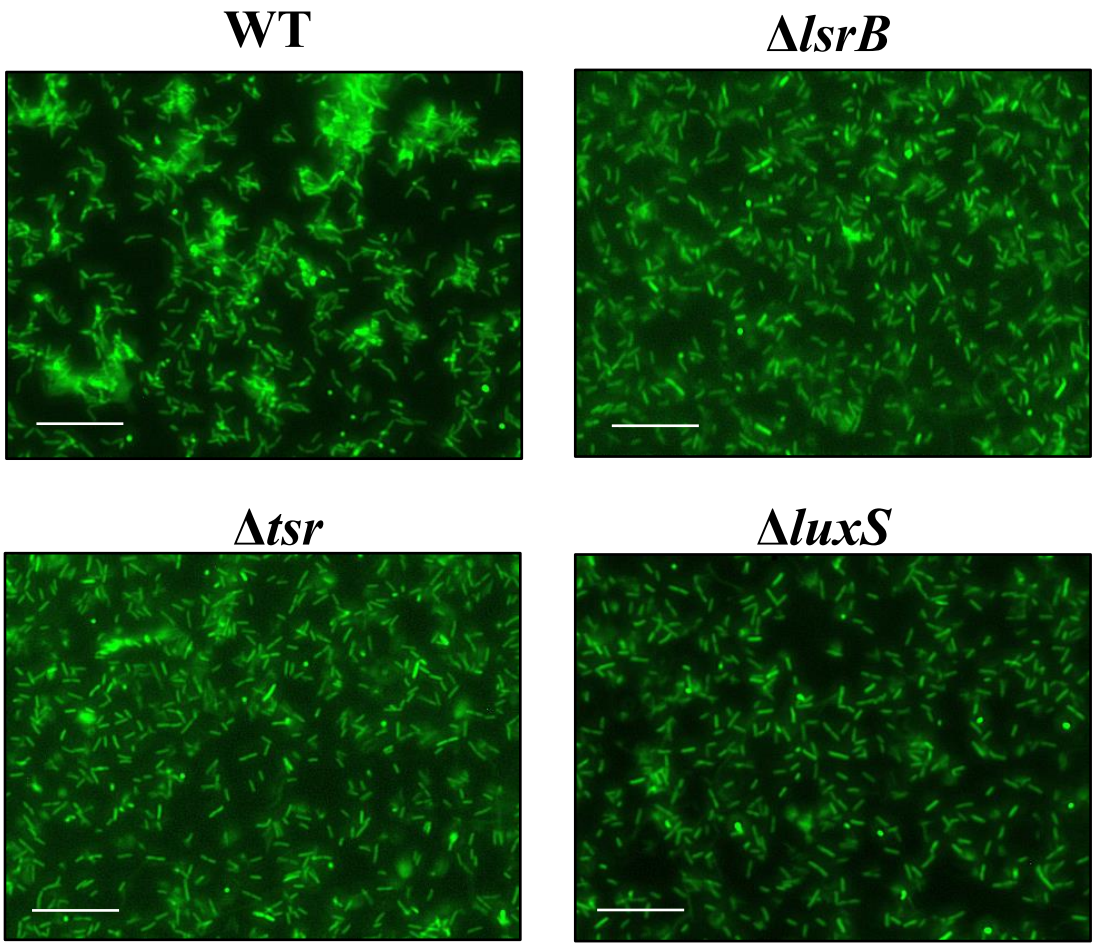

Figure 10: Self-aggregation on the surface after 2 h at 30°C. WT and isogenic Δ*lsrB*, Δ*tsr*, and Δ*luxS* mutants diluted to 10^7 cell/mL in ABTCAA medium were seeded into polystyrene, incubated at 30°C, and the bottom surface of the wells was imaged at 2 h. Images from four biological replicates were acquired. Images shown here (462 x 346 pixels) are from a section of a representative image (1388 x 1040 pixels). Scale bar = 25 µm.

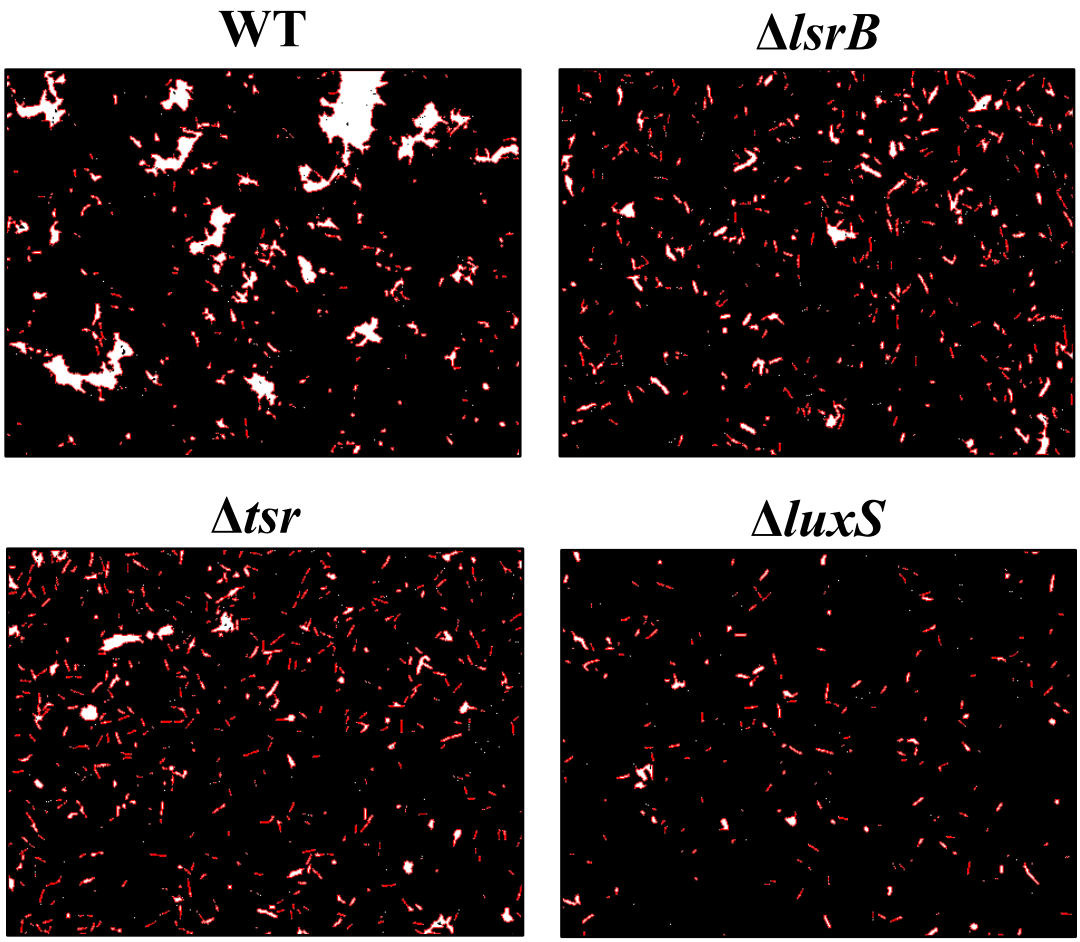

Figure 11: Threshold images showing aggregates larger than 50 pixels. Images of WT and isogenic Δ*lsrB*, Δ*tsr*, and Δ*luxS* mutants were thresholded using the image analysis program. Aggregates larger than 50 pixels were generated and outlined in red in the threshold images. Images shown here correspond to the images in Figure 10.

$$Fraction\ of\ pixels\ in\ aggregates = \frac{Sum\ of\ pixels\ in\ aggregates}{Total\ number\ of\ pixels\ in\ image}$$

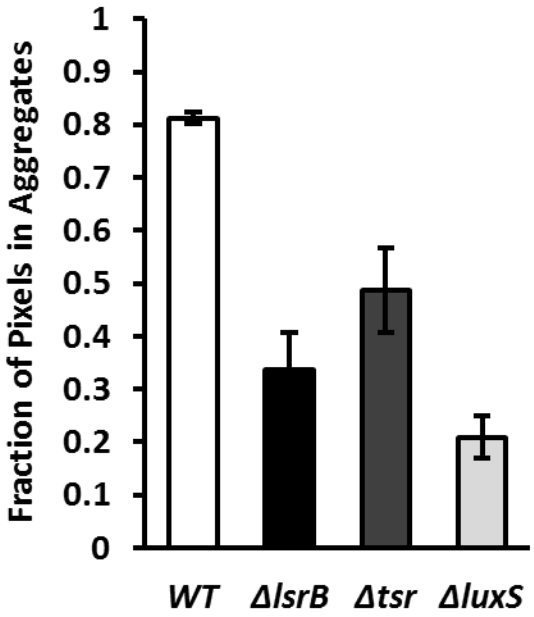

Figure 12: Histogram depicting the percentage of pixels in aggregates after 2 h at 30°C. The fraction of pixels in aggregates were determined using the equation above the chart. The values are averages of one image each from four biological replicates. Error bars represent the standard error of the mean of the replicates.

Self-aggregation continued to progress in WT over 12 h at 30°C as seen in the representative images in Figure 13. Δ*lsrB*, Δ*tsr* and Δ*luxS* cells appear to be defective in self-aggregation and form smaller aggregates as compared to WT. The differences in self-aggregation are clearly evident between 4-8 h, when most of the growth and self-aggregation occurs in contact with the surface. Large microcolonies appear by 12 h.

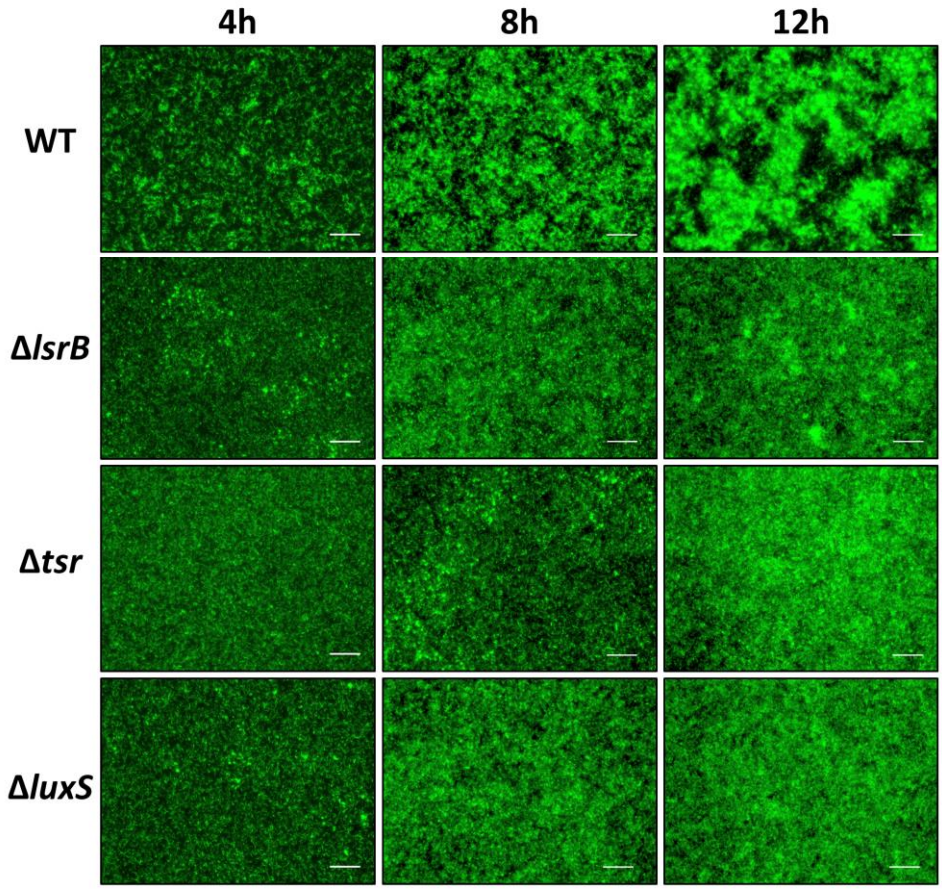

Figure 13: Self-aggregation over 12 h at 30°C. WT, Δ*lsrB*, Δ*tsr*, and Δ*luxS* cells were grown and seeded into 96 well plates as described in Methods. Time (h) of imaging is indicated above each column and represents the duration of incubation at the specified temperature. One well each for four biological replicates were imaged at the specified time points. Images shown are representative of the specified time point. Scale bars = 50 µm.

The quantitative analysis of the images support visual observations. A larger fraction of pixels are present in aggregates for WT cells as compared to Δ*lsrB*, Δ*tsr* and Δ*luxS* cells (Figure 14). Quantitative analysis of all the images between 4-12 h was done using a defined threshold aggregate size of 350 pixels. Comparing all the images using the same threshold allowed following the progression of the increase in aggregate size over 12 h (compare histogram for each strain as a function of time in Figure 14). By 12 h of incubation, cells in all strains are distributed in the Z direction as well as in the X-Y plane. The fluorescence microscope used captures two-dimensional images and hence, the detailed features of three-dimensional growth are not clear. Additionally, cell movement results in the appearance of blurry halos around cells. The quantitative analysis program cannot effectively distinguish between unclear features, halos, and actual self-aggregates. This results in a smaller difference in fraction of pixels in aggregates between WT and the mutants at 12 h.

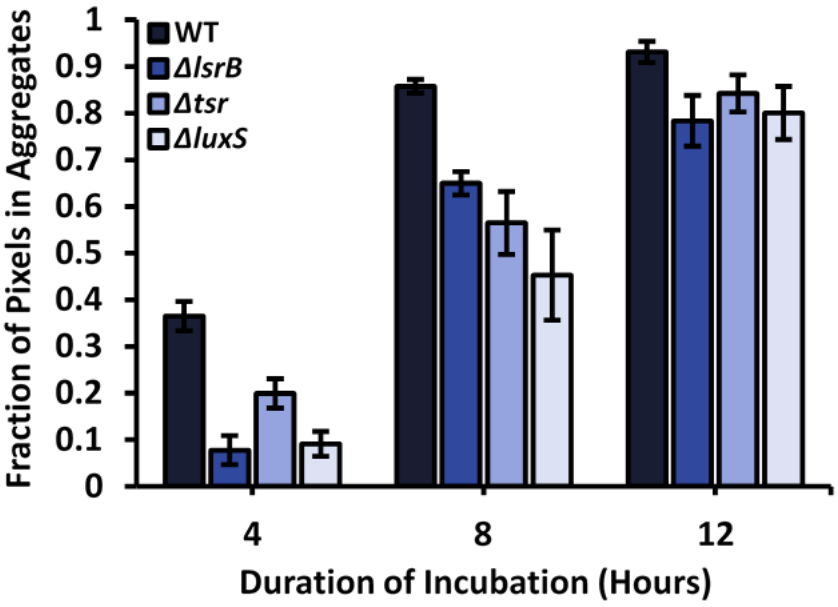

Figure 14: Histogram depicting the percentage of pixels in self-aggregates on the surface between 4-12 h at 30°C. Threshold aggregate sizes were set at 350 pixels. The fraction values are averages of one image each from four biological replicates. Error bars represent the standard error of the mean of the replicates.

A similar pattern of self-aggregation on the surface is also observed at 37°C (Figure 15). The aggregates are larger in size for WT and grow in the Z plane at a faster rate. Several small aggregates close to each other were observed Δ*lsrB*, Δ*tsr* and Δ*luxS* cells. A threshold aggregate size of 450 pixels was used to quantify the fraction of pixels that were present in aggregates. A majority of the pixels in the threshold images for the WT cells belong in aggregates above the threshold size (Figure 16). Only 20% or fewer of the pixels are found in aggregates for Δ*lsrB*, Δ*tsr* and Δ*luxS* at 4 h. There is rapid

growth in the Z plane after 4 h, which probably accounts for the diminished differences between WT and the mutants thereafter.

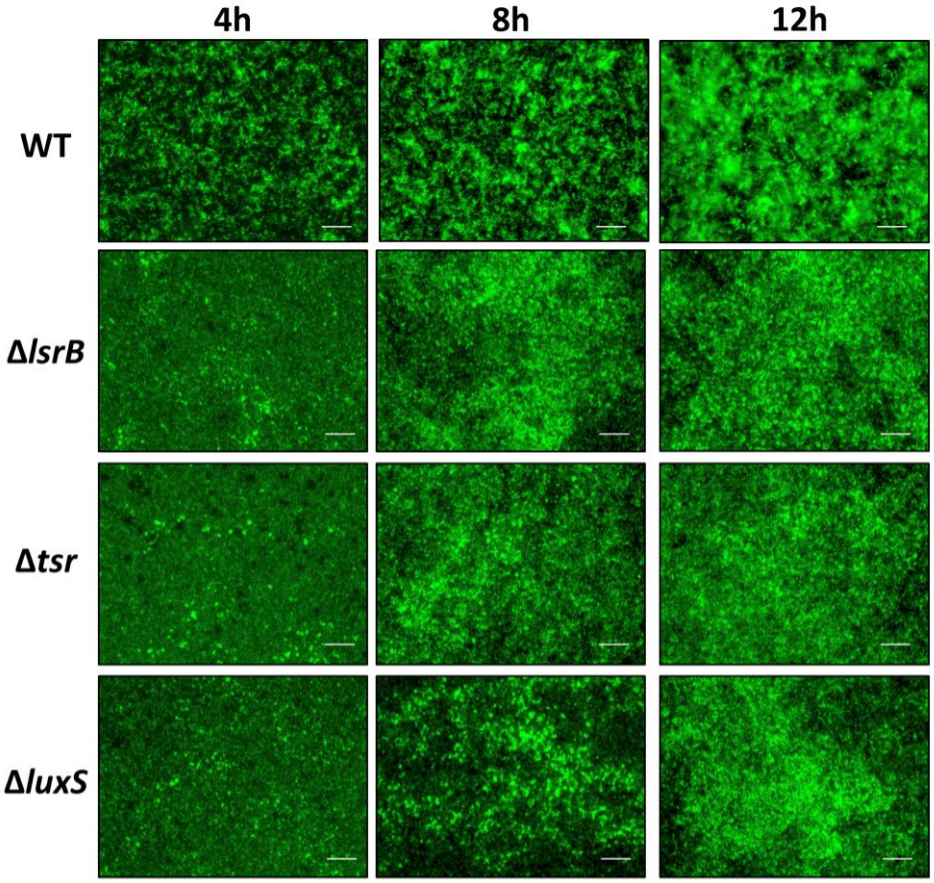

Figure 15: Self-aggregation over 12 h at 37°C. WT, Δ*lsrB*, Δ*tsr*, and Δ*luxS* cells were grown and seeded into 96 well plates as described in Methods. Time (h) of imaging is indicated above each column and represents the duration of incubation at the specified temperature. One well each for four biological replicates were imaged at the specified time points. Images shown are representative of the specified time point. Scale bars = 50 µm.

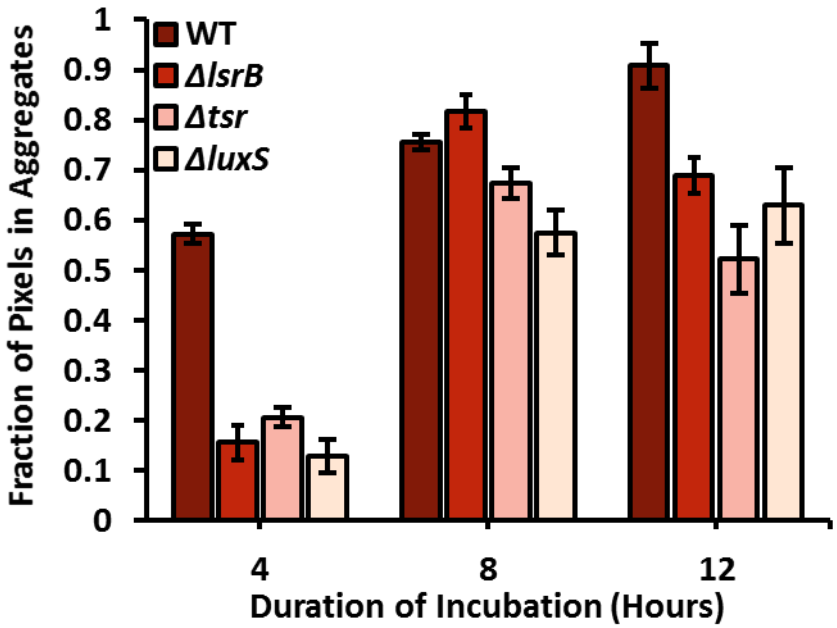

Figure 16: Histogram depicting the percentage of pixels in self-aggregates on the surface between 4-12 h at 37°C. Threshold aggregate sizes were set at 450 pixels. The fraction values are averages of one image each from four biological replicates. Error bars represent the standard error of the mean of the replicates.

Determination of AI-2 levels in the culture medium

To determine if AI-2 is present extracellularly under the specified growth conditions, I assayed the bulk medium for AI-2 every 4 h from the time of seeding. I used the *V. harveyi* bioluminescence assay for AI-2 detection (111). Upon sensing AI-2 present in the medium, *V. harveyi* produces light that can be detected using a luminometer. This assay is strictly qualitative as a number of factors including pH and nutrient composition

affect the extent of light production (112). As seen in Figure 17A, light emission in response to AI-2 was only detected for Δ*lsrB* which is defective in AI-2 uptake, and to a much lesser extent, for Δ*tsr* at 12 h at 30°C. As cells grow faster at 37°C, extracellular AI-2 accumulation occurred sooner at this temperature. AI-2 begins to accumulate in the bulk medium of the Δ*lsrB* at 8 h, and is detected in the bulk medium of all the AI-2 producing strains at 12 h (Figure 17B). AI-2 was not detected in the bulk medium for any of the strains at 4 h. These data do not definitively indicate that AI-2 is not present at the earlier time points as there are several factors that could affect AI-2 detection including variation in diffusion of molecules under shaking versus static conditions and AI-2 production in bulk medium versus at the surface.

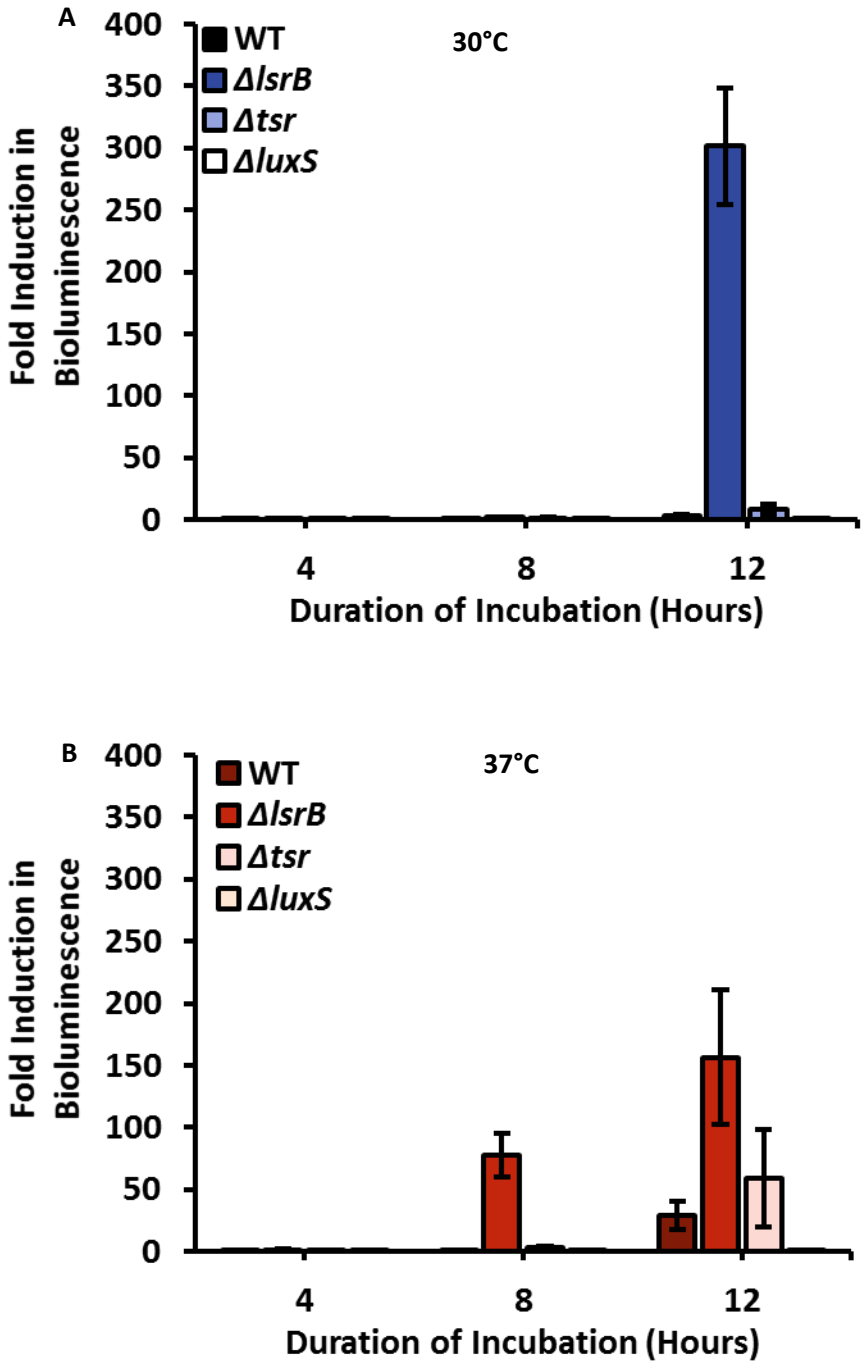

Figure 17: AI-2 accumulation in bulk medium between 4-12 h. WT, Δ*lsrB*, Δ*tsr*, and Δ*luxS* were grown to the specified time points and culture fluids were collected from wells at 30°C (A) or 37°C (B) as described in methods. Luminescence detected is expressed as Relative Light Units per second. Data shown are averages of three independent replicate wells. Error bars represent the standard error of the mean of the replicates.

Chemotaxis, aggregation, and biofilm formation of AI-2 uptake and processing mutants

In *E. coli,* AI-2 is imported into the cell via the LsrACDB transport apparatus. Once inside, it is phosphorylated by the kinase LsrK. Phospho-AI-2 then binds to the repressor LsrR to relieve repression of the divergently transcribed *lsrACDBFG* and *lsrRK* operons. Thus, AI-2 accumulation leads to expression of LsrACDB to import AI-2 and LsrFG to degrade P-AI-2 (Figure 4). Using microarrays to determine the early stationary phase transcription profile of LsrR and LsrK knockouts, Li *et al* found that the role of LsrR and LsrK extends beyond their involvement in AI-2 processing. That study demonstrated that LsrR and LsrK perceive the internalized AI-2 signal and affect the expression of downstream genes that are involved in regulating aggregation, attachment, and biofilm formation and architecture (7). LsrR and LsrK also affect the expression of the *lsr* operon, and hence, internalize AI-2 faster (Δ*lsrR*) or slower (Δ*lsrR*) than wild-type *E. coli* (44). It follows that these strains contain different amounts of LsrB in their periplasm as compared to WT. I hypothesized that different levels of LsrB in the periplasms of Δ*lsrR* and Δ*lsrK* mutants would affect their ability to respond to self-generated AI-2 and in turn affect self-aggregation during early biofilm development. I also tested a Δ*lsrC* mutant as it is able to respond normally to an external AI-2 gradient but is slightly defective in AI-2 uptake (11, 44).

I isolated periplasmic protein from Δ*lsrC*, Δ*lsrR* and Δ*lsrK* mutants and used immunoblotting to detect the LsrB present in these strains. Figure 18 shows the immunoblot with periplasmic LsrB from WT, Δ*lsrC*, Δ*lsrR*, and Δ*lsrK* cells. The results

show that at OD_{600nm} = 0.5, the periplasm of Δ*lsrC* cells contains about the same of LsrB as WT, Δ*lsrR* cells contains 700% more LsrB than that of WT cells, and the Δ*lsrK* mutant contains only 20% of the LsrB present in WT cells.

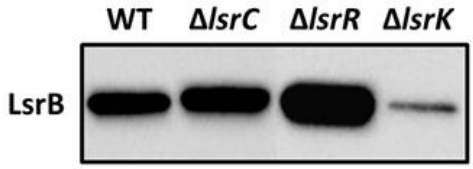

Figure 18: Immunoblot with LsrB in periplasmic fractions of WT, Δ*lsrC*, Δ*lsrR*, and Δ*lsrK*. Cells were growth to OD_{600nm} = 0.5 in TB medium at 30°C, 250 rpm. Periplasmic contents were isolated using the osmotic shock method as previously described. 20 µg of total periplasmic protein was loaded into each lane and immunoblotting was performed as described in Methods. The blot is representative of three independent experiments.

The chemotaxis response of these strains to an external AI-2 gradient is shown in Figure 19. The AI-2 dose-response curve of the Δ*lsrC* and Δ*lsrR* strain is similar to that of the WT strain. The Δ*lsrK* strain, on the other hand, appears to be slightly defective in sensing an external AI-2 gradient. AI-2 chemotaxis has previously been shown to be independent of AI-2 uptake into the cell, as a LsrC mutant performs normal chemotaxis toward AI-2 (11). An LsrABCD channel uptake mutant is, however, not as deficient in

AI-2 import as an Δ*lsrK* mutant (113). It is likely that the combined effect of defective AI-2 uptake during growth and low levels of LsrB affect chemo-sensing an external AI-2 gradient. The Δ*lsrK* mutant, as well as all of the other *lsr* and *luxS* mutants, respond normally to 10 mM *L*-serine (data not shown), suggesting that changes in Tsr expression or function are not responsible for the decreased AI-2 chemotaxis response of Δ*lsrK*.

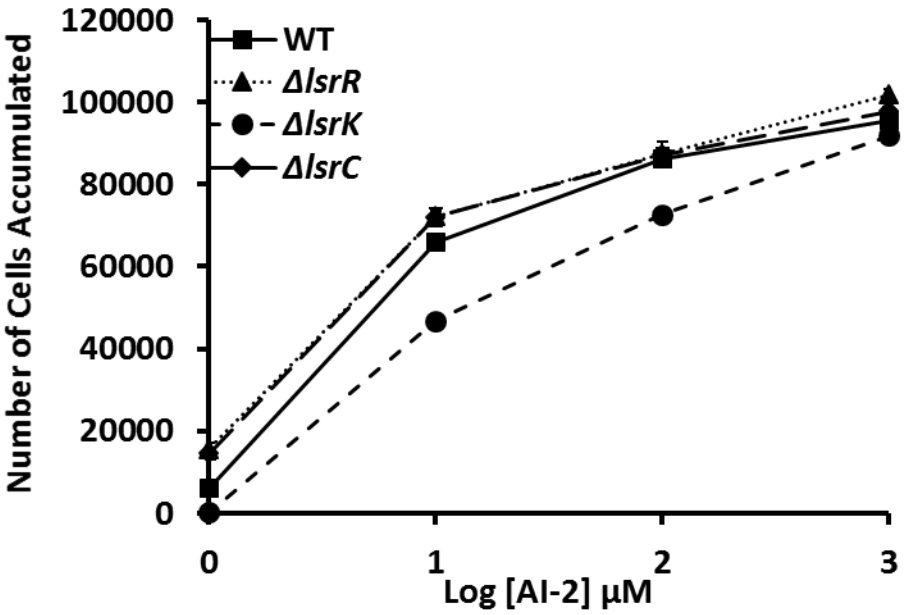

Figure 19: Chemotaxis response of WT, Δ*lsrC*, Δ*lsrR,* and Δ*lsrK cells* to 1-1000 µM AI-2 in the capillary assay. Capillary assays were performed at 30°C as described in Methods. Data shown are averages of nine capillaries from three independent experiments. The Y axis represents the background-subtracted accumulation of cells in the capillary. Error bars represent the standard error of the mean for three biological replicates.

The ΔlsrR, ΔlsrK, *and* ΔlsrC *mutants are defective in biofilm formation and aggregation on a surface*

Previous studies have observed defects in biofilm architecture, biomass and thickness in Δ*lsrR* and Δ*lsrK* mutants in flow cells (7), whereas the effect of knocking out *lsrC* on biofilm development is unknown. I used the crystal violet assay to determine if biofilms formed by these mutants are defective in attachment to the surface of polystyrene plates. As seen in Figures 20A and 20B, Δ*lsrR,* Δ*lsrK* and Δ*lsrC* cells attach less strongly than WT cells to polystyrene at 24 h at 30°C and 37°C respectively. The results with Δ*lsrR* and Δ*lsrK* strains support previous observations by other groups.

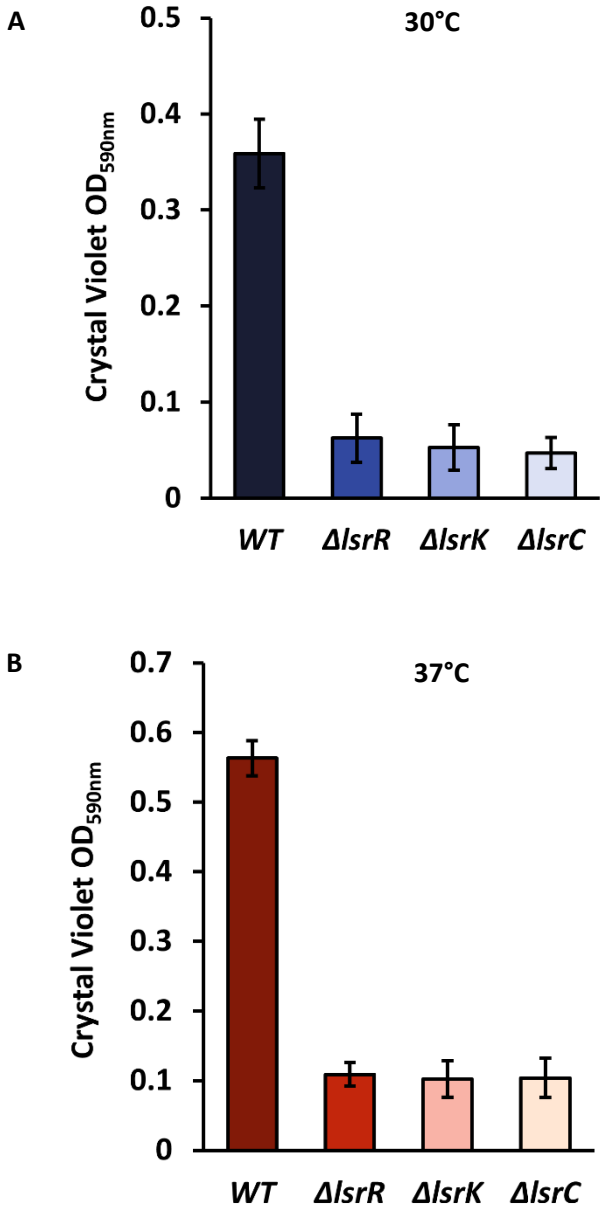

Figure 20: Quantification of attached biofilm biomass of WT, *ΔlsrR*, Δ*lsrK*, and Δ*lsrC* using the crystal violet assay. WT, *ΔlsrR*, Δ*lsrK*, and Δ*lsrC* cells were seeded in 96 well polystyrene plates as described in Methods and were incubated for 24 h at 30°C (A) or 37°C (B). Data shown are averages of five replicate wells each for six biological replicates. Error bars represent the standard error of the mean for the replicates.

To test whether the defect in forming strongly attached biofilms was influenced by effects seen early on in self-aggregation on a surface I tested self-aggregation of WT, Δ*lsrC*, Δ*lsrR*, and Δ*lsrK*. I used 8-chambered wells that have a glass coverslip bottom surface instead of polystyrene. The coverslip bottom allows acquisition of clear images as it is thinner than polystyrene. However, unlike in the polystyrene wells, the cells tend to move toward the edges of the well. This leads to crowding and more growth along the edges as compared to the center. The non-uniformity affects the time at which self-aggregates appear in the center.

I acquired images from at 12 h at 37 °C. Representative images are shown in the left panel of Figure 21. WT shows the presence of large self-aggregates whereas Δ*lsrR,* Δ*lsrK*, and Δ*lsrC* have cells that cluster close together but do not form large aggregates. The panel on the right shows aggregates larger than a threshold aggregate of 350 pixels. These threshold images correspond to the colored images in the left panel. Figure 22 shows the fraction of pixels present in aggregates in the threshold images. Only ~20-30% of the pixels are present in aggregates for Δ*lsrR*, Δ*lsrK,* and Δ*lsrC* strains as compared to ~70% for WT. These results suggest that although these strains are capable of sensing AI-2 normally, they are unable to trigger downstream signaling events that that promote self-adherence.

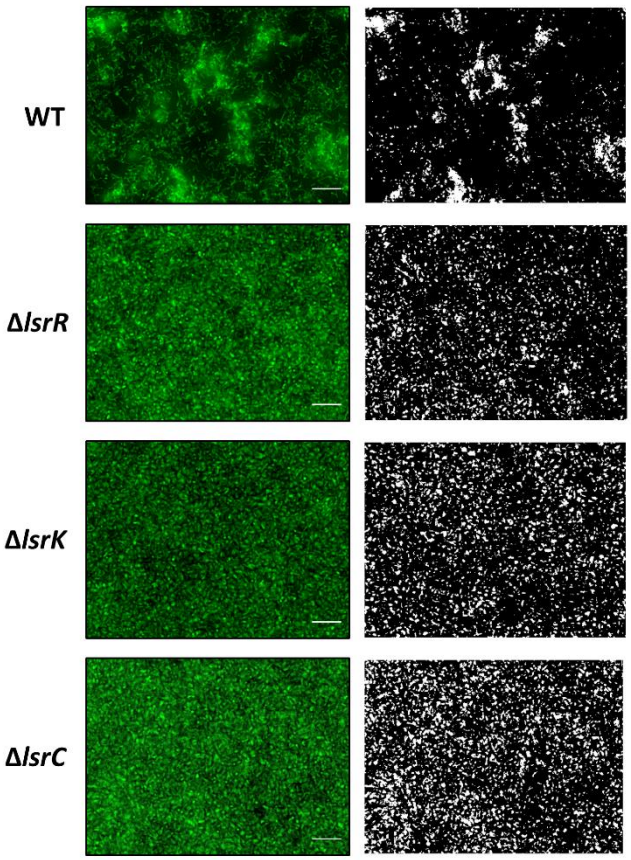

Figure 21: Self-aggregation of WT and isogenic Δ*lsrR*, Δ*lsrK*, and Δ*lsrC* mutants on the surface after 12 h at 37°C. Cells were diluted to 10^7 cell/mL in ABTCAA medium were seeded into 8 chamber wells, incubated 37°C, and the bottom surface of the wells was imaged at 12 h. The panel on the left shows representative image sections (462 x 346 pixels) of two biological replicates. Scale bar = 25 µm. The panel on the right shows corresponding threshold images acquired using a threshold pixel size for aggregates set to 350 pixels.

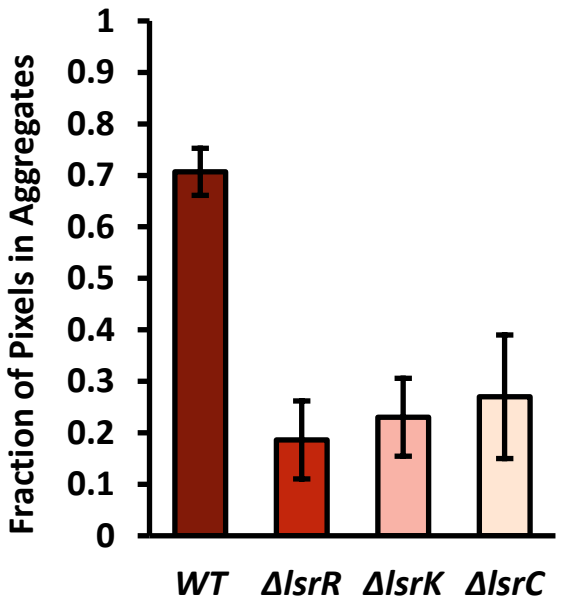

Figure 22: Histogram depicting the fraction of pixels in aggregates of WT and isogenic Δ*lsrR*, Δ*lsrK*, and Δ*lsrC* mutants on the surface after 12 h at 37°C. The fraction values are averages of two images each from two biological replicates. Error bars show the standard error of the mean for the replicates.

The ΔlsrR *and* ΔlsrK *mutants are normal for curli production*

In *E. coli*, surface attachment is affected by the expression of adhesion factors such as type I fimbriae and curli fibers as well as self-recognizing surface autotransporter adhesins such as Ag43 (114). For example, curli fibers have been shown to enhance biofilm formation by facilitating interactions between cells and the surface as well as among cells (115-118). The curli regulatory protein CsgD has also been shown to repress the expression of regulatory flagellar genes, thereby promoting surface

attachment (80, 119). As the Δ*lsrR* and Δ*lsrK* deletion mutants are normal for chemotaxis to an external AI-2 gradient and appear to form tiny self-aggregates on the surface, I tested the possibility that the defects observed in self-aggregation are due to defects in regulation and expression of adhesive factors such as curli fibers. To test this hypothesis, I assayed the production of curli fibers using the congo red colony assay. In this assay, strains are streaked on a plate containing congo red. If they produce curli fibers, the colony color turns red. Colonies of all the strains began appearing reddish 24 h after incubation at 30°C or 37°C. Figures 23 A and B shows representative images for WT, Δ*lsrR* and Δ*lsrK* strains 72 h after incubation at 30°C and 37°C respectively. These data suggest that there are no differences in curli production among the strains and that differences in the number of curli fibers present are probably not a factor in the differences in self-aggregation and attachment seen with the strains under study.

A

B

Figure 23: Curli production of WT, Δ*lsrR*, and Δ*lsrK* in the congo red assay. Strains were cultured on YESCA congo red plates as described in Methods and incubated at either 30°C (A) or 37°C (B). Images shown are representative of three independent replicates.

II. 5 Discussion

In this study, I demonstrated that WT forms cellular aggregates on an abiotic surface in a similar manner at 30°C and 37°C. Self-aggregation appears to require AI-2 chemotaxis, as Δ*lsrB* and Δ*tsr* cells aggregate at a slower rate on the surface and fewer cells are found in aggregates in these strains (Figures 10-16). My results support the observations by Park *et al* that showed, under restrictive conditions, cells depend on Tsr-dependent chemotaxis to aggregate (120) and that the aggregation might be mediated by attraction to self-released molecules.

AI-2 is a self-attractant, as recently shown by Laganenka *et al* (121), and sensing it requires both LsrB and Tsr (11). It is, therefore, likely that the deficiency in aggregation of the Δ*tsr* and Δ*lsrB* mutants is a result of the inability of cells to sense AI-2 and promote attraction to one another. The Δ*luxS* mutant, which does not synthesize AI-2, is also defective in cellular aggregation. It can respond to external gradients of both *L*-serine and AI-2 (this study, chapter III) and presumably other Tsr-dependent attractants. However, as the Δ*luxS* strain presumably produces any other self-generated attractants besides AI-2, this result demonstrates that none of these molecules is sufficient to induce self-aggregation. The Δ*luxS* strain also has other metabolic defects in addition to the absence of AI-2, and these could potentially contribute to defective biofilm development (45, 122). It is possible that the Δ*lsrB* and Δ*tsr* mutations may also have pleiotropic effects that were not investigated in this study.

AI-2 was not detected in the bulk medium in the wells prior to 12 h at 30°C and 8 h at 37°C with either WT or the deletion mutants (Figure 17A and B). However, as the cells aggregate and attach to the surface, they begin producing EPS, which may slow down the diffusion of molecules away from the cells, so non-homogenous distribution of AI-2 could also affect the detection of AI-2. While examining the aggregation kinetics of *E. coli* W3110, Laganenka *et al* found that a P_{lsr}-*egfp*-expressing vector that produces GFP in response to the presence of AI-2 is more active in aggregates as compared to planktonic cells (121), so it remains possible that some AI-2 is localized in the aggregates prior to the time points it was detected at in the bulk medium.

Several studies have suggested that aggregation leads to the establishment of locally high cell densities that exceed the threshold necessary for initiating QS-dependent biofilm formation (86, 120, 123). My results support this view as strains that were defective in AI-2 chemotaxis and aggregation during early stages of biofilm development also had lower surface-attached biofilm biomass (Figure 7A and B).

Chemotaxis to external AI-2 by the Δ*lsrR* mutant, which this and a previous study (45) have shown to be deficient in self-aggregation and biofilm formation, was identical to that of WT cells, although this strain produces 700% more LsrB than WT (Figures 18 and 19). The Δ*lsrR* mutant does not form large aggregates like WT on a surface nor attach strongly to the surface (Figures 20-22). Li *et al* found that the expression of *csgE*, a curli production assembly/transport protein, was ~3-fold lower in a Δ*lsrR* strain relative to WT (7). However, I did not observe any deficiency in curli

production in the Δ*lsrR* strain after 72 h (Figure 23). Li *et al* studied expression using early stationary phase cultures of *E. coli* W3110 grown in LB. Both the strains used and difference between suspended cells and cells growing on an agar surface could have contributed to the different outcomes. The reasons for the decreased aggregation of the Δ*lsrK* mutant, which produces only 20% as much LsrB as WT cells, and the Δ*lsrR* mutant remain unknown. However, one might speculate that a finely tuned balance must exist between AI-2 production and LsrB production for optimal self-aggregation. In this view - assuming that AI-2 production remains unaffected by the Δ*lsrK* and Δ*lsrR* mutations, the Δ*lsrK* strain may produce too little LsrB and the Δ*lsrR* strain may produce too much.

The Δ*lsrC* mutant contains about the same amount of LsrB in its periplasm as WT. This result was somewhat surprising as LsrC is part of the AI-2 uptake channel; if AI-2 is not internalized normally, the *lsrB* containing *lsr* operon should remain repressed. However, it has been previously observed that the initial internalization of AI-2 occurs via the phosphoenolpyruvate system (113). Nonetheless, despite containing WT levels of LsrB and responding to an external gradient of AI-2 normally, the Δ*lsrC* strain is deficient in self-aggregation and surface attachment. This result suggests that chemotaxis to AI-2 alone is not be enough to trigger biofilm development.

Data obtained from experiments comparing the behavior of WT cells with the behavior of Δ*lsrB,* Δ*tsr* and Δ*luxS* mutants suggests that AI-2 chemotaxis enhances self-aggregation and biomass attachment to a surface. Data obtained from experiments

comparing the behavior of WT cells with Δ*lsrR*, Δ*lsrK* and Δ*lsrC* cells show that AI-2 chemotaxis is sufficient to bring cells close to an external AI-2 source. However, our results suggest that AI-2 chemotaxis per se is insufficient to promote self-aggregation and surface attachment. This could be because of more stringent requirements for chemotaxis-mediated self-attraction of planktonic cells or because the mutants have defects in downstream pathways that are required for aggregations and stable surface attachment. In conclusion, this work implies that a fully functional AI-2 QS system is required to coordinate responses from chemotaxis with downstream signaling events that lead to collective behavior. The complexity of this system suggests that there are multiple steps in the process that may be targets for therapeutic intervention.

CHAPTER III

ANALYSIS OF FACTORS INFLUENCING CHEMOTAXIS TOWARD AN EXOGENOUS AI-2 GRADIENT

III.1 Overview

E. coli senses the bacterial interspecies quorum-sensing signal AI-2 as a chemoattractant. The response to AI-2 requires interaction between the periplasmic binding protein LsrB and the *L*-serine chemoreceptor Tsr. In this study, AI-2 chemotaxis was assayed as a function of the amount of LsrB during culture growth to understand the dependence of AI-2 chemotaxis on binding protein levels. Mid-exponential phase cells growing in tryptone broth sense an external AI-2 gradient optimally when the cellular LsrB level is ~250 molecules. However, cells at this growth stage containing as few as 50-70 copies of LsrB still perform essentially normal AI-2 chemotaxis. In comparison, there are 3,000-5,000 copies of Tsr monomer per cell at OD_{600nm} = 0.5. Thus, a low ratio of LsrB:Tsr is sufficient to elicit a strong chemotaxis response. Cells are less responsive to external AI-2 at later growth stages (OD_{600nm} = 0.7 and 0.9), although their responses to *L*-serine remain nearly unchanged. Because Δ*luxS* cells that do not produce AI-2 also show a decreased response to AI-2 at later stages of growth, jamming of the system by self-produced AI-2 cannot be the full explanation for this phenomenon. Also, cells are minimally responsive to AI-2 when they have the highest levels of periplasmic LsrB. Thus, the reason(s) for the decreased response at later stages of growth is unknown,

although changes in chemoreceptor ratios and other metabolic changes may be contributing factors.

III.2 Introduction

The chemotaxis machinery in *E. coli* allows cells to sense gradients of various attractant and repellent chemicals (nutrients and toxins), pH, temperature, and oxygen in their environment (51) and to move in a favorable direction within these gradients. This sensory information presumably guides cells to specific niches within their environment. Research on bacterial chemotaxis grew rapidly in the late 1960s and the 1970s. After the initial classification of chemoattractants and chemorepellents by Julius Adler and others (124-128), most of the work focused on understanding how the chemotaxis two-component signal transduction system perceived, integrated, and relayed information about those gradients (51, 64, 129-131). In recent years, identification of niche-specific chemoeffectors has increased rapidly. One of the goals of research on this topic is to understand how these chemoeffectors regulate behavior and colonization of organisms in their preferred environment (9, 11, 27-29, 54, 56). In this study, I focused on understanding the mechanism underlying chemotaxis toward a specific bacterial signal called AI-2. AI-2 is likely to be present in numerous environments, including soil, food and water sources, and several sites within the human body as it is produced by a multitude of Gram-positive and Gram-negative bacteria (132, 133).

In *E. coli*, chemotaxis toward an external AI-2 gradient occurs once AI-2-bound LsrB interacts with the chemoreceptor Tsr (11). This is the first example of Tsr sensing a

ligand indirectly. Several other molecules are sensed indirectly via a substrate-binding protein interacting with a chemoreceptor, including maltose by Tar, ribose and glucose/galactose by Trg, and dipeptides by Tap (57, 59, 60, 134). The interaction between ligand-bound maltose-binding protein (MBP) and the chemoreceptor Tar has been studied extensively (57, 135-137) and provides the basis for investigating the interaction between AI-2-bound LsrB and Tsr. Optimal chemotaxis toward maltose requires the presence of a large amount of MBP in the periplasm (up to 50,000 copies per cell), and Tar and the maltose transport system compete for binding of MBP. MBP binds maltose with high affinity which sequesters it in the periplasm, but the maltose-MBP complex binds Tar (~4000 copies/cell; (138)) with low affinity (estimated K_D of ~200 μM), which allows cells to migrate to high concentrations of maltose (57).

Chemotaxis toward AI-2 has also been shown to be independent of the LsrACD uptake system (11). However, AI-2 is not an effective carbon source (2, 20, 22) and presumably there is no benefit acquired from sequestering it. Furthermore, AI-2 has been proposed to have a relatively low binding affinity for LsrB (~160 μM) (139), although this measurement in highly uncertain because of the equilibrium that exists between three different forms of AI-2, only one of which is sensed by LsrB (20). Therefore, I hypothesized that the dependence of AI-2 chemotaxis on the periplasmic level of LsrB is likely to be different than the dependence of chemotaxis to maltose on the level of MBP. The current study was undertaken to determine this dependence and to understand its

significance. I believe this information will allow us to better understand the physiological importance of chemotaxis toward AI-2 in *E. coli*.

III.3 Materials and Methods

Bacterial strains, chemicals, and growth media

The strains and plasmids used in this study are listed in Table 3. All strains were derived from wild-type *E. coli* RP437 (referred to as WT from here on) (91). Cells were grown in tryptone broth medium (TB; 10 g/L tryptone, and 8 g/L NaCl) at 30°C, 250 rpm for capillary assays and osmotic shock protein extraction. Luria-Bertani medium (140) was used for $P1_{vir}$ transduction. The medium was supplemented with antibiotics as necessary. Chemically synthesized DPD (linear form of AI-2, spontaneously converts to cyclized form) purchased from Dr. Rita Ventura at ITQB, Oeiras, Portugal (141) was used in capillary assays. *L*-serine was purchased from VWR (USA).

Construction of isogenic deletion mutants

Deletion mutants were constructed using $P1_{vir}$ transduction as previously described with some modifications (94). Briefly, BW25113 single-gene knockout mutants carrying the Km^R cassette (93) were infected with $P1_{vir}$ that had been previously propagated in WT to maintain an isogenic background. Liquid lysates were collected and used to infect WT. WT Km^R insertion mutants were selected for on LB agar plates containing 50 µg/mL kanamycin, 50 µg/mL streptomycin and 10 mM sodium citrate (pH 5.5). Each mutant was then verified using colony PCR with two sets of primers: forward (F) and reverse

(R) gene primers, and forward (F) gene primer and K1 reverse primer. PCR verification primers used are listed in Table 4. The strains were transformed with the FLP recombinase carrying plasmid pCP20 to eliminate Km^R cassette resulting in clean deletion mutants (95, 96).

Table 3: Strains and plasmids used in this study.

Strain name in text	**Relevant genotype or phenotype[a]**	**Reference**
WT	*E. coli* RP437 Stm^R	(91)
Δ*luxS*	*E. coli* RP437Δ*luxS* Km^S Stm^R	This study
Vibrio harveyi TL-26	Δ*luxN* Δ*luxS* Δ*cqsS*	(104)
Plasmids		
pET15b-*lsrB*	Expression vector, Amp^R	This study

[a] Stm – streptomycin, Km – kanamycin, Amp – ampicillin

Table 4: Primers used for PCR verification of Km^R insertion mutants.

Primer Name	**Sequence (5'- 3')**	**Source**
K1	CAGTCATAGCCGAATAGCCT	(95)
*luxS*_F	GGAAAAACACGCCTGACAGAAAAG	This study[a]
*luxS*_R	GGGCTGGTGTGGTTTGCTAA	This study[b]

[a] F = forward or upstream primer
[b] R stands for reverse or downstream primer

Purification of E. coli *LsrB for antibody production*

E. coli LsrB expressed from pET15b-*lsrB* (kindly provided by Frederick Hughson, Princeton University) in strain BL21(DE3) was purified using affinity chromatography followed by size exclusion chromatography. Purified LsrB without the histidine tag (His) was used to generate anti-LsrB antibody in goat. Briefly, the strain was grown to OD_{600nm} = 0.5 in LB medium with 100 µg/mL ampicillin at 37°C, 250 rpm. Cells were induced with 3 mM IPTG (VWR, USA) and grown overnight to overexpress *lsrB*. The cells were harvested and frozen at -80°C. Frozen cells were thawed at room temperature and resuspended in 50 mL equilibration buffer (50 mM Tris base, 0.3 M NaCl, pH 8.0). Cells were lysed by sonication, centrifuged, and the clear supernatant was run through a column containing equilibrated Ni-NTA resin (Qiagen, USA; bed volume = 5 mL). The column was washed twice with equilibration buffer to eliminate non-specific proteins. A 0-500 mM imidazole gradient was used to collect 2mL fractions. Fractions containing LsrB-His were pooled and introduced into a HiLoad Superdex 75 PG column (GE Healthcare Life Sciences, USA). The His tag was cleaved using Thrombin CleanCleave (Sigma, USA). The purified protein was sent to Bethyl Laboratories, Inc. (Texas, USA) for polyclonal antibody production in goat. The polyclonal antibody obtained was purified using protein A beads (NEB, USA) and used for detecting LsrB.

Osmotic shock for periplasmic protein extraction

Periplasmic fractions were extracted from cells using the osmotic shock protocol developed by Neu and Heppel (142). Briefly, cells were grown to OD_{600nm} = 0.5 at 30°C in 500 mL TB and harvested by centrifugation at 10,000 x *g* for 15 minutes at 4°C. The pellet was resuspended in 100 mL of osmotic shock buffer (30 mM pH 8.0 Tris-HCl, 20% sucrose and 1 mM pH 8.0 EDTA) and incubated on gyrotory shaker at 180 rpm for 10 min at room temperature. The suspension was centrifuged at 13,000 x *g* 15 min at 4°C. The pellet was resuspended in 50 mL ice cold ultrapure water and incubated in an ice bath shaker at 180 rpm for 10 min to release the periplasmic contents. The suspension was centrifuged again and the supernatant was carefully collected and concentrated to 1mL using a 10,000 MWCO centrifugal filter (Millipore, USA). Total protein concentration was determined using the BCA assay (Thermo Scientific, USA).

Immunoblotting for detection of LsrB

Immunoblotting using antibody generated against LsrB was performed with the periplasmic isolates to detect and quantify LsrB. SDS-PAGE was performed as previously described (143) followed by wet transfer (Mini-Trans Blot Electrophoretic Transfer Cell, BioRad, USA) for 1 h at 100 V onto low fluorescence PVDF membrane (Thermo Scientific, USA). The membrane was first blocked with blocking buffer (3% non-fat dry milk, TBST (10 mM pH 7.5 Tris-HCl, 100 mM NaCl, 0.1% Tween 20)), followed by incubation with primary antibody (anti-LsrB antibody, 1:2500 in blocking

buffer), and then secondary antibody (anti-goat HRP, 1:50,000 in blocking buffer). Incubations were performed at room temperature with continuous agitation. The membranes were washed thoroughly with TBST (3x, 5 min each) after incubation with primary and secondary antibodies. A StainFree blot image was captured using the ChemiDoc Touch Imaging System (BioRad, USA). This image was used for total protein normalization in each lane. The blot was developed using Clarity ECL substrate (BioRad, USA) and a chemiluminescent image was acquired. Total protein normalization and estimation of relative LsrB levels were performed using ImageLab software (BioRad, USA).

Determination of chemotaxis response using capillary assays

Capillary assays were carried out as previously described (102) with the following modifications for preparing cells before introducing them into chemotaxis chambers. Cells were centrifuged at 600 x *g* for 10 min, followed by gentle resuspension in a volume of chemotaxis buffer (CB, 1X phosphate-buffered saline, 100 µM EDTA, 1 µM L-methionine, and 10 mM lactic acid, pH 7.4) such that the final OD_{600nm} = ~0.5. The tubes were then placed on a low-speed tube roller at 30°C for 15 min before being introduced into the chemotaxis chambers. Number of cells accumulated in the capillary was determined by subtracting the accumulation of cells in capillaries containing only CB from the accumulation of cells in capillaries containing the attractant.

Vibrio harveyi *bioluminescence assay*

V. harveyi strain TL-26 was used to detect AI-2 activity in cell-free culture fluids as previously described (101). For obtaining cell-free culture fluids, an overnight culture of WT was back diluted to OD_{600nm} = 0.05 in TB, placed in plastic culture tubes (1 mL per tube, 1 tube per time point), and incubated at 30°C, 250rpm. At the desired time point, a fraction of the culture was used to measure cell density, and the remaining culture was centrifuged at 16,100 x*g* for 10 min at 4°C. The cell-free culture fluid was collected and used in the bioluminescence assay. 10% cell-free supernatant was added to 90% TL-26 culture (overnight culture diluted 1:5000 in AB medium) in an opaque white 96-well plate (Greiner Bio-One, USA) and incubated at 30°C for 4 h. The luminescence (490 nm) from each well was read using the Mithras LB940 Multimode Microplate reader (Berthold, USA). Luminescence output from the reader is expressed as Relative Light Units (RLU) per second. Luminescence output of the control wells, i.e., TB medium only, is negligible at this time point. The luminescence of the samples is represented as fold induction in bioluminescence which is obtained by background normalizing the sample RLU.

III.4 Results

AI-2 regulates various density-dependent behaviors, including biofilm formation, in several Gram-positive and Gram-negative bacteria that produce it (reviewed in (26)). AI-2 produced by one species can also regulate the behavior of another species. For example, Xavier and Bassler (39) found that *V. harveyi* responds to AI-2 produced by *E. coli* by inducing bioluminescence, and AI-2 made by *V. harveyi* induces the AI-2 regulated *lsrACDBFG* operon in *E. coli*. Some bacterial species, such as *H. pylori* and *E. coli* are also able to detect AI-2 in their environment using the two-component chemotaxis system. *H. pylori* senses AI-2 as a repellant, whereas *E. coli* senses it as an attractant (11, 28). Chemotaxis to endogenous AI-2 facilitates biofilm formation (this study, (121)). As *E. coli* can sense AI-2 produced by a different species, it is possible that exogenous AI-2 can guide *E. coli* to non-self sources of AI-2, thereby promoting the formation of mixed species communities. In this section, I determine the parameters involved in sensing an exogenous AI-2 gradient.

Dose-dependent response to an exogenous AI-2 gradient

In vitro chemotaxis assays such as the capillary assay are designed to study chemotaxis toward one molecule to determine the concentration range in which the molecule is detected. They typically separate motile cells from the medium that they are grown in before using them in the assay to prevent interference from other molecules that may be present in the medium. As AI-2 is produced by bacteria, it is possible that some of it might be present in the cytoplasm and periplasm, and consequently be secreted into the buffer in which the cells are maintained in during the assay. Therefore, I tested whether self-produced AI-2 interferes with chemotaxis toward an external gradient by comparing the chemotaxis response of AI-2-producing WT cells with a Δ*luxS* mutant that cannot make AI-2. Mid-exponential phase are very motile and cells from this phase are usually used in chemotaxis studies. The chemotaxis response of mid-exponential phase WT and Δ*luxS* cells follows a similar dose-response curve, as seen in Figure 24. Both strains are able to sense AI-2 over a wide concentration range (1-1000 μM). The response approaches saturation beyond 100 μM. Figure 25 shows that WT cells are accumulating endogenously produced AI-2 extracellularly at this growth stage (OD_{600nm} = 0.5, T = 3 h) and it follows that some of it is present intracellularly. Culture fluids from Δ*luxS* cells do not induce bioluminescence of *V. harveyi* at any stage of growth as they do not synthesize AI-2 (data not shown).

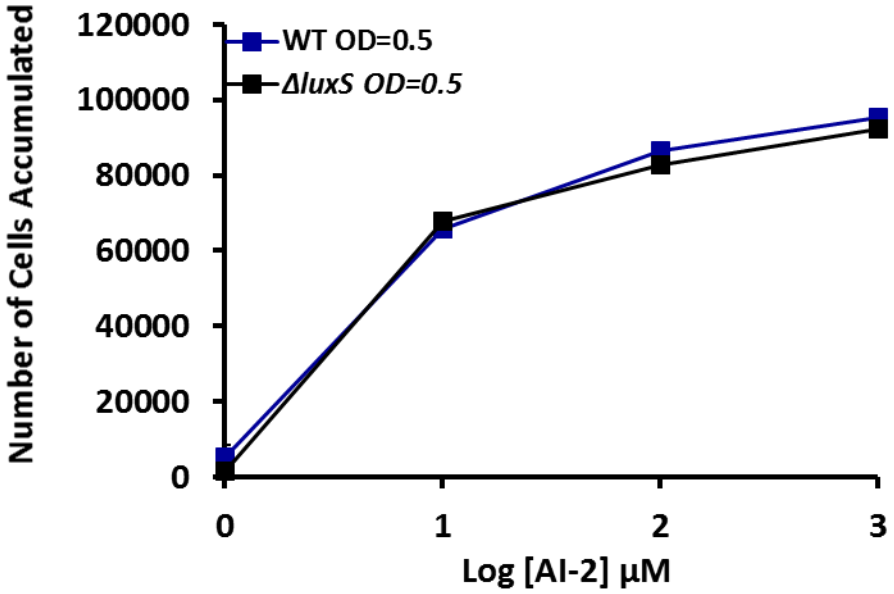

Figure 24: Chemotaxis response of mid-exponential phase WT and Δ*luxS* strains to 1-1000 µM AI-2. Capillary assays were performed at 30°C with cells in mid-exponential phase (OD_{600nm} = 0.5). Results shown are averages of six capillaries from two independent experiments. The Y axis represents background subtracted accumulation of cells in the capillary. Error bars represent standard error of mean for two biological replicates.

AI-2 continues to be released extracellularly beyond mid-exponential phase as seen in Figure 25. It peaks in late-exponential phase (OD_{600nm} = 0.7, T = 4 h) and is rapidly internalized during early stationary phase (OD_{600nm} = 0.9, T = 5 h). Presumably, there is more AI-2 present in the cells at later stages of growth and hence, I tested the chemotaxis response of both WT and Δ*luxS* cells at OD_{600nm} = 0.7 and OD_{600nm} = 0.9.

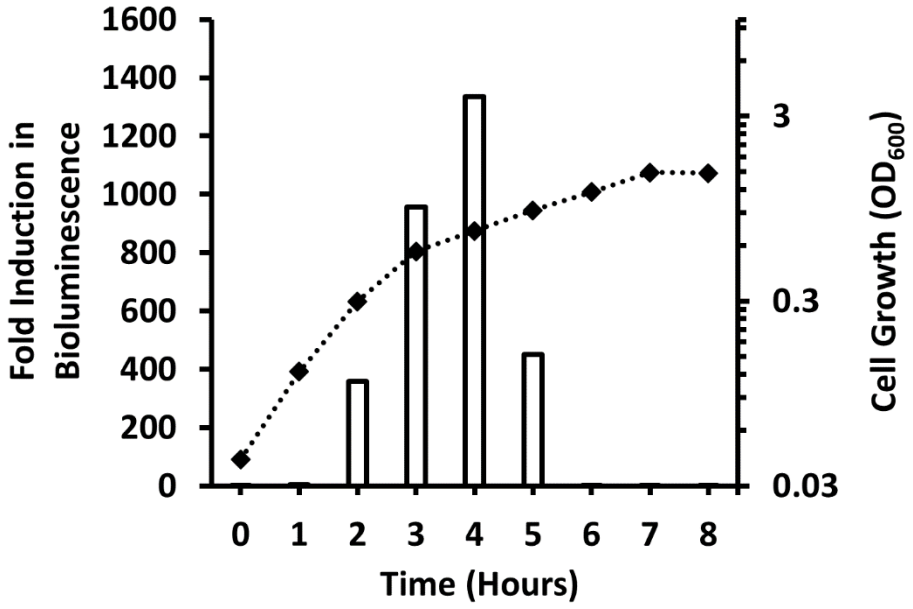

Figure 25: Growth-dependent AI-2 accumulation in WT culture fluids at 30°C. WT cell were cultured under shaking conditions in TB medium. Cell density was recorded every hour (black diamonds), and cell-free supernatant was collected for testing AI-2 levels in culture fluids as described in Methods. The presence of AI-2 leads to induction of luminescence in the reporter strain TL26 which is represented as background normalized fold induction on the left Y-axis (clear bars). Data shown are from one independent replicate.

As seen in Figure 26, the chemotaxis responses of OD_{600nm} = 0.7 and OD_{600nm} = 0.9 cells are drastically lower than those of OD_{600nm} = 0.5 cells. Interestingly, the response of both WT and Δ*luxS* cells decreases to the same extent. These data suggest that, under the conditions tested, self-produced AI-2 does not interfere with sensing and responding to an external AI-2 gradient. Rather, other factors must specifically inhibit AI-2 chemotaxis during later growth phases.

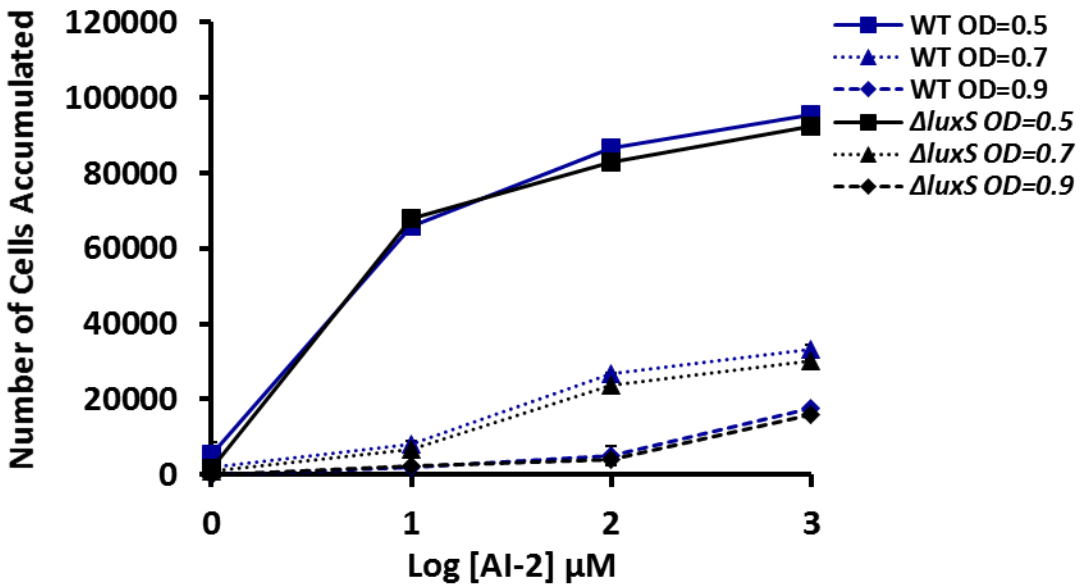

Figure 26: Growth stage-dependent chemotaxis response of WT and Δ*luxS* strains to AI-2. Capillary assays were performed at 30°C with 1-1000 µM AI-2. Results shown are averages of six capillaries from two independent experiments. The Y axis represents background subtracted accumulation of cells in the capillary. Error bars represent standard error of mean for two biological replicates.

The ratio of Tar:Tsr present in the receptor patch changes as a function of growth (144). Tsr senses *L*-serine directly and therefore, I tested the response of WT and Δ*luxS* cells at the different growth stages to *L*-serine to determine whether functional Tsr availability was a reason for the decrease in AI-2 chemotaxis at later growth stages. As seen in Figure 27, the response of both strains to *L*-serine is similar and mostly unchanged at both strains at OD_{600nm} = 0.5, OD_{600nm} = 0.7 and OD_{600nm} = 0.9.

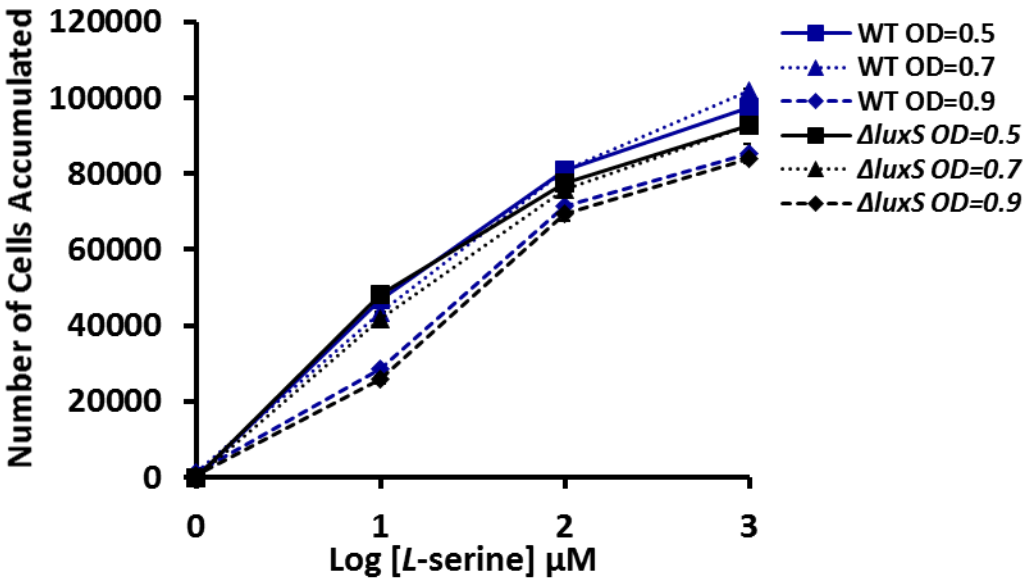

Figure 27: Growth stage-dependent chemotaxis response of WT and Δ*luxS* strains to *L*-serine. Capillary assays were performed at 30°C with 1-1000 µM *L*-serine. Results shown are averages of six capillaries from two independent experiments. The Y axis represents background subtracted accumulation of cells in the capillary. Error bars represent standard error of mean for two biological replicates.

In *E. coli*, the *lsr* operon produces the components required for internalizing and degrading AI-2. This operon is induced as the cells grow from mid-exponential to stationary phase (44). The decrease in the response of WT cells seen at later growth stages could be related to an increase in the amount of the LsrB protein, which interacts with Tsr after binding AI-2. To test this hypothesis, I isolated periplasmic fractions at mid-exponential (OD_{600nm} = 0.5), late-exponential (OD_{600nm} = 0.7), and early-stationary phase (OD_{600nm} = 0.9) for both strains and performed immunoblotting for LsrB detection.

The immunoblot with LsrB from WT and Δ*luxS* strains grown to the specified optical densities is shown in Figure 28. The LsrB bands seen in the Δ*luxS* mutant are a result of the background of uninduced expression of the *lsr* operon. The amount of LsrB present in Δ*luxS* cells is similar at OD_{600nm} = 0.5 and OD_{600nm} = 0.9; a modest increase is seen at OD_{600nm} = 0.7. It is possible that nutrient depletion in the medium and subsequent metabolic shifts affect the expression of the *lsr* operon in this strain, thereby changing in the amount of periplasmic LsrB present. In WT cells, LsrB levels are quite similar at OD_{600nm} = 0.5 and OD_{600nm} = 0.7, although there is a two-fold decrease at OD_{600nm} = 0.7 as compared to OD_{600nm} = 0.5 (Table 5). There is a drastic increase in LsrB at OD_{600nm} = 0.9, which presumably facilitates the rapid removal of AI-2 from the medium. Visual observations match the normalized volume intensities obtained. Using the normalized values, I determined the amount LsrB present in the strains relative to WT OD_{600nm} = 0.5 (Table 5).

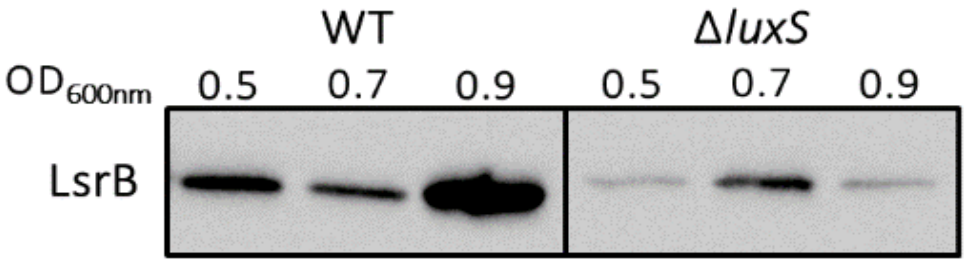

Figure 28: Immunoblot with LsrB in periplasmic fractions of WT and Δ*luxS* strains at different growth phases. Cells were grown to the specified densities and periplasmic protein was extracted as described in Methods. Cells at OD_{600nm} = 0.5 are in mid-exponential phase, cells at OD_{600nm} =0.7 are in late-exponential phase, and cells at OD_{600nm} = 0.9 are in early stationary phase. Each lane contains 20 µg of total periplasmic protein. Data shown are from one independent replicate.

Table 5: Amount of LsrB relative to WT cells at OD_{600nm} = 0.5.

Strain	OD_{600}	Relative amount of LsrB
WT	0.5	1
WT	0.7	0.5
WT	0.9	5.3
Δ*luxS*	0.5	0.2
Δ*luxS*	0.7	0.4
Δ*luxS*	0.9	0.2

* The relative amount of LsrB (ng) reflects the amount present in 20µg of total periplasmic protein. These data were acquired by normalizing the volume intensities obtained for the bands in Figure 28 with the volume intensity of WT cells at OD_{600nm} = 0.5. Data are from one independent experiment.

Comparing the relative levels of LsrB with AI-2 chemotaxis responses of WT and Δ*luxS* cells at all stages of growth, and especially at OD_{600nm} = 0.9, I find that Δ*luxS* cells respond in the same manner as WT cells to AI-2 even though they have only 20% as much LsrB in their periplasm. Based on these results, it does not appear that the decrease in AI-2 chemotaxis response seen in WT and Δ*luxS* cells at later growth stages depends on the amount of LsrB present in the periplasm. Other factors must affect the chemotaxis response to AI-2 at later growth stages. Whatever the true explanation is for the reduced chemotaxis to AI-2 after mid-exponential phase, its seems that the LsrB:Tsr ratio present in cells at that growth phase is optimal for sensing an external AI-2 gradient, and that higher LsrB:Tsr ratios or lower Tsr:Tar ratios negatively affect the response to AI-2.

Quantification of periplasmic LsrB in mid-exponential phase cells

There are an estimated ~3000-5000 copies of Tsr monomer per cell at mid-exponential phase (138, 145). To determine the ratio of LsrB to Tsr at OD_{600nm} = 0.5, I quantified the amount of LsrB present in the periplasm in WT and Δ*luxS*. Immunoblotting was performed with a range of concentrations of purified LsrB to compare with periplasmic fractions from five WT isolates (Figure 29A). A linear standard concentration curve was generated for the purified LsrB using the volume intensity obtained from the blot (Figure 29B). I then calculated the total number of molecules of LsrB per cell. The calculations (Figure 29C) show that the periplasm contains 240-360 copies of LsrB during mid-exponential phase. I used this information to extrapolate the amount of LsrB present in

the Δ*luxS* mutant. As it contains ~20% as much LsrB in its periplasm compared to WT, Δ*luxS* cells are capable of responding to an external AI-2 gradient with as few as 50-70 copies of LsrB per cell. This result indicates that an LsrB:Tsr ratio as low as 1:100 is sufficient to elicit a chemotaxis response to an external AI-2 gradient.

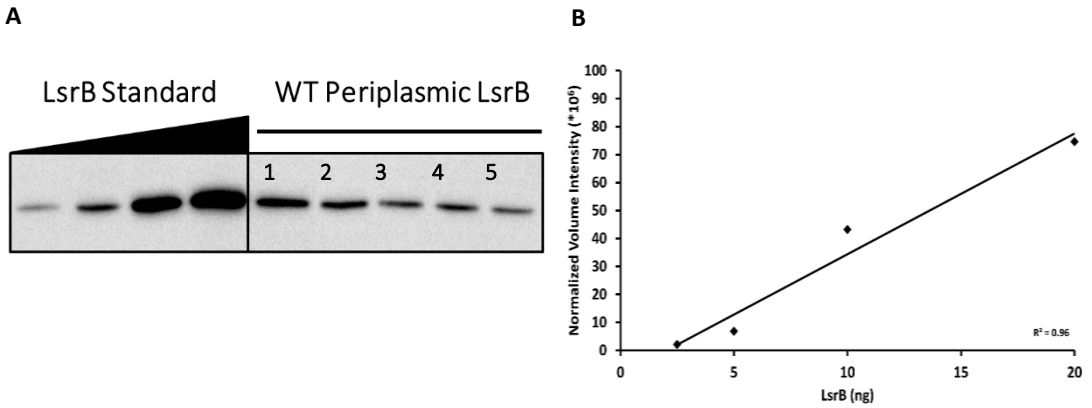

C

Amount of LsrB in WT

Amount of LsrB/cell = Total periplasmic protein per cell x amount of LsrB in each lane = $2.2*10^{-17}$ g/cell

Molecular mass of LsrB = $3.7*10^{4}$ g/mol

Moles of LsrB per cell = $2.2*10^{-17}$ g/cell x 1 mol/$3.7*10^{4}$ g = $6*10^{-22}$ moles/cell

Molecules of LsrB per cell = $6*10^{-22}$ * $6*10^{23}$ = 360

Figure 29: Quantification of periplasmic LsrB in WT. A) Immunoblot with purified LsrB (From L to R: 2.5ng, 5ng, 10ng, 20ng) and periplasmic fractions from five WT isolates (10 µg per well). B) Standard curve obtained by plotting the normalized volume intensity obtained versus the amount of LsrB. C) Calculations for determining the amount of LsrB per cell. The example shown is for replicate # 1, which gives the highest amount of LsrB. The range for all five replicates is 240-360 molecules per cell.

III.5 Discussion

In this study, I demonstrated that mid-exponential phase WT cells respond to an external AI-2 gradient in the capillary assay in a concentration-dependent manner, with the response approaching saturation after 100 µM AI-2 in the capillary (Figure 24). Saturation was not observed even at the highest concentration of AI-2 (3.3 mM) tested in the first published report on AI-2 chemotaxis (11). This difference might reflect the source of AI-2 used. The results reported here are supported by a recently published study that used the same AI-2 source to test the chemotaxis response of *E. coli* W3110 cells to an AI-2 gradient in a microfluidic device (44). That study reported saturation at 200µM AI-2 (121).

The AI-2 chemotaxis response of WT cells is not affected by endogenous AI-2, as a Δ*luxS* strain that does not make AI-2 responds equally well to an external AI-2 gradient (Figure 24), even though it possesses only 20% as much LsrB per cell as the WT strain at OD_{600nm} = 0.5 (Figure 28, Table 5). A notable phenomenon is that the chemotaxis response to AI-2 peaks in these cells, which are in mid-exponential phase, and then declines dramatically at OD_{600nm} = 0.7 and even more so at OD_{600nm} = 0.9 (Figure 26), whereas *L*-serine chemotaxis is essentially the same at all of these growth phases (Figure 27). This effect is seen with both WT and Δ*luxS* cells, although they have very different levels of periplasmic LsrB; as much as 50 fold more in WT cells at OD_{600nm} = 0.9 (Figure 28, Table 5). Thus, there is no obvious correlation between either the ability to self-produce AI-2 or the periplasmic level of LsrB to explain the decrease at later growth

stages. Kalinin *et al* have shown that the Tar:Tsr ratio increases steadily after OD_{600nm} = 0.5 (144). It is, therefore, possible that the decrease at later growth stages is due to the decreasing relative amount of Tsr in the receptor patch, a possibility that I am now testing. However, it is equally likely that some other, more complex metabolic response is responsible. Whatever the explanation may be, it appears that cells are maximally attracted to AI-2 during exponential growth and before they would be expected to undergo any density-dependent metabolic adjustments.

AI-2 chemotaxis requires both LsrB and Tsr (11). The amount of Tsr present in mid-exponential phase cells has been previously characterized as 3,000-5,000 copies per cell. I quantified the amount of LsrB in WT and Δ*luxS* cells in order to determine the relative amounts of LsrB and Tsr that are required for optimal AI-2 chemotaxis. The periplasm of WT cells contain about 240-360 copies of LsrB per cell (Figure 29), and Δ*luxS* cells contain about 20% of that amount. Thus, an impressively low ratio of LsrB:Tsr, ~1:100, is sufficient to sense exogenous AI-2 with a dose-response relationship like that of the WT cells (Figure 24). In comparison, sensing and responding to a maltose gradient optimally requires an excess of binding protein compared to the chemoreceptor. Optimal maltose sensing requires about 50,000 molecules of maltose binding protein (MBP) per cell and 3,000 molecules of the chemoreceptor Tar per cell (57). Maltose has a high binding affinity for MBP and maltose bound MBP has a low affinity for Tar. As maltose is a nutrient it makes sense that the cells contain an excess of MBP as it allows sequestering maltose in the periplasm. The low binding affinity of

MBP:maltose and Tar facilitates swimming toward high concentrations of maltose. AI-2, on the other hand, is not a nutrient, it is a signal. There is obvious benefit to sequestering AI-2 in the periplasm and hence, it makes sense that cells need a very low amount of LsrB to sense AI-2. The low ratio of LsrB:Tsr seems to be sufficient to significantly amplify the signal from indirect binding of AI-2 to Tsr. These data support our hypothesis that LsrB and Tsr interact with very high affinity. *In vitro* binding studies with purified components will be required to determine the actual binding affinity.

I conclude that *E. coli* does not depend on induction of the AI-2-dependent QS system to sense and swim toward higher concentrations of AI-2, meaning that cells at low density still respond to pre-existing gradients of AI-2, such as those produced by biofilms or other dense cell aggregations. Only after joining these bacterial communities, which can be composed of any of the many bacteria that produce AI-2, would the induction of AI-2-dependent metabolic, structural, and behavioral changes occur. Thus, AI-2 could constitute a homing signal for isolated planktonic *E. coli* cells.

CHAPTER IV

FUTURE DIRECTIONS

V.1 Investigation of the Role of Chemotaxis to AI-2 in the Formation of Biofilms by Adherent Invasive *E .coli*

This study shows that chemotaxis to endogenous AI-2 promotes surface attachment in the non-pathogenic K-12 derivative strain *E. coli* RP437. It would be interesting to determine whether AI-2 chemotaxis also promotes attachment of *E. coli* pathobionts such as adherent invasive *E .coli* (AIEC). AIEC attachment and subsequent proliferation in the intestines of patients suffering from inflammatory conditions such as Crohn's disease has been shown to contribute to the pathogenesis of the disease (reviewed in (146). Investigating this relationship could allow identification of new targets for combating AIEC progression in the gut. The *in vitro* setup described in Chapter II of this study could be used to perform a proof-of-concept experiment. If AIEC and its isogenic Tsr and LsrB mutants show the same results as *E. coli* RP437, their attachment to a biotic surface, such as the *in vitro* epithelial cell line HT-29, could be studied.

V.2 Investigation of the Role of Chemotaxis to Non-self AI-2 in the Formation of Multi-species Communities

This study shows that chemotaxis to endogenous AI-2 promotes biofilm formation. In nature, multi-species biofilms are far more common than mono-species biofilms. As AI-2 is an interspecies signal, it would be interesting to determine whether AI-2 produced by one species can attract cells of another species, thereby leading to the establishment of communities composed of more than one bacterial species. A simple *in vitro* model could be used to test co-aggregation of different species. A GFP-tagged strain that produces AI-2 or does not produce AI-2 (lacks *luxS*) would be introduced into a 96 well plate or microfluidic flow device. The strains would be allowed to form biofilms and the time point at which AI-2 is detected in the extracellular medium of the AI-2 producing biofilm would be noted. The second strain that is RFP-tagged and does not produce AI-2 would be introduced at this time point. Confocal microscopy or culturing methods could be used to determine whether the second strain co-aggregates better with the AI-2 producing strain or the non-AI-2-producing strain. This setup could, for example, be used to investigate whether *Campylobacter jejuni* and *E. coli* co-aggregate in an AI-2 chemotaxis-dependent manner. *C. jejuni* causes enteritis after establishing itself in the human GI tract. AI-2 signaling has been shown to be required for its colonization in chickens (disease carrier) (147). *C. jejuni* is deficient in colonizing and infecting healthy adult mice, but infant mice with an underdeveloped microbiota or adult mice that suffer from intestinal inflammation are highly susceptible to it. These mice also have high

loads of commensal *E. coli* (148). The chemotaxis response of *C. jejuni* to AI-2 is not known. It is possible that AI-2 is an attractant for *C. jejuni*, and it can sense AI-2 released by commensal *E. coli* and swim toward it. Such a cue could allow *C. jejuni* to reach a niche it can successfully colonize. *C. jejuni* produces AI-2 but does not internalize it (149), and hence, it could in turn attract *E. coli* toward it leading to the proliferation of inflammation inducing communities in the gut.

CHAPTER V

SUMMARY

In this study, I found that chemotaxis toward AI-2 enhances self-aggregation on a surface, which in turn facilitates biofilm formation (Chapter II). Cells do not need to produce AI-2 to sense and swim up an AI-2 gradient, but they need to be able to produce AI-2 to form aggregates and surface attached biofilms. It remains to be seen whether Δ*luxS* mutants can join aggregates if they are present in a mixed population that also contains AI-2 producing cells. Self-aggregation depends on the AI-2 binding protein LsrB, the Tsr chemoreceptor, and the AI-2 uptake and processing components LsrC, LsrR and LsrK. A diagram presenting a model for the role of chemotaxis toward AI-2 in the context of self-aggregation on a surface, attachment to the surface, and biofilm formation is shown in Figure 30.

Chemotaxis toward AI-2 could potentially draw one bacterial species to aggregations of another, leading to the formation of multi-species biofilms, which are a common occurrence in nature. It could also promote the movement of individual cells within an established biofilm toward a metabolically active site at which AI-2 is being released. The results from Chapter III show that recognizing an exogenous AI-2 gradient in independent of endogenous AI-2 production. This supports the idea that non-self AI-2 acts as a ‘universal call’ for attracting free swimming cells. Understanding the influence of AI-2 chemotaxis on the onset of self-aggregation and biofilm formation could allow

development of therapeutics with novel targets to combat infections caused by pathogenic or opportunistic *E. coli*.

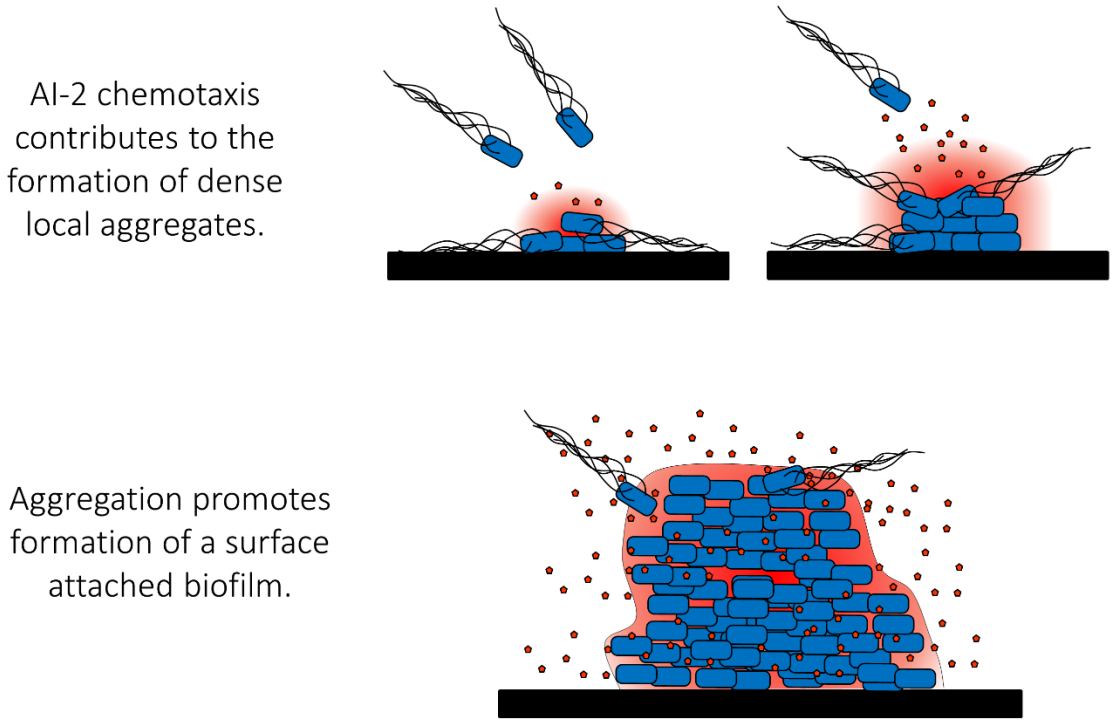

Figure 30: Model for role of AI-2 chemotaxis in self-aggregation and biofilm formation. Top panel: Bacteria entering a new environment, such as the lumen of the GI tract, must establish themselves in a suitable location by outcompeting forces (fluid flow, enzymes, peristalsis, and the immune system) that are designed to flush them out. The substratum (black bar) represents a prime location for establishment of a thriving population of incoming cells. Flagellar rotation and other mechanical and chemical cues allow cells to sense the surface and attach reversibly. AI-2 (red pentagons) gradients (red halos) emanating from reversibly attached cells attract free-swimming cells toward (L). This behavior leads to the formation of clumps of cells closely connected together (aggregates) (R). Bottom panel: Aggregates are locally high in cell density. This high cell density exceeds the threshold necessary to induce AI-2-dependent quorum-sensing processes such as formation of surface attached formation. These biofilms potentially continue to attract free swimming cells as long as they produce AI-2.

REFERENCES

1. Marques JC, Lamosa P, Russell C, Ventura R, Maycock C, Semmelhack MF, Miller ST, Xavier KB. 2011. Processing the interspecies quorum-sensing signal autoinducer-2 (AI-2): characterization of phospho-(S)-4,5-dihydroxy-2,3-pentanedione isomerization by LsrG protein. J Biol Chem 286:18331-43.
2. Marques JC, Oh IK, Ly DC, Lamosa P, Ventura MR, Miller ST, Xavier KB. 2014. LsrF, a coenzyme A-dependent thiolase, catalyzes the terminal step in processing the quorum sensing signal autoinducer-2. Proc Natl Acad Sci U S A 111:14235-40.
3. Sourjik V. 2004. Receptor clustering and signal processing in *E. coli* chemotaxis. Trends Microbiol 12:569-76.
4. Hartl DL, Dykhuizen DE. 1984. The population genetics of *Escherichia coli*. Annu Rev Genet 18:31-68.
5. Blount ZD. 2015. The unexhausted potential of *E. coli*. Elife 4.
6. Leimbach A, Hacker J, Dobrindt U. 2013. *E. coli* as an all-rounder: the thin line between commensalism and pathogenicity. Between Pathogenicity and Commensalism 358:3-32.
7. Li J, Attila C, Wang L, Wood TK, Valdes JJ, Bentley WE. 2007. Quorum sensing in *Escherichia coli* is signaled by AI-2/LsrR: effects on small RNA and biofilm architecture. J Bacteriol 189:6011-20.

8. Niu C, Robbins CM, Pittman KJ, Osborn j L, Stubblefield BA, Simmons RB, Gilbert ES. 2013. LuxS influences *Escherichia coli* biofilm formation through autoinducer-2-dependent and autoinducer-2-independent modalities. FEMS Microbiol Ecol 83:778-91.

9. Bansal T, Jesudhasan P, Pillai S, Wood TK, Jayaraman A. 2008. Temporal regulation of enterohemorrhagic *Escherichia coli* virulence mediated by autoinducer-2. Appl Microbiol Biotechnol 78:811-9.

10. Kendall MM, Rasko DA, Sperandio V. 2007. Global effects of the cell-to-cell signaling molecules autoinducer-2, autoinducer-3, and epinephrine in a *luxS* mutant of enterohemorrhagic *Escherichia coli*. Infect Immun 75:4875-84.

11. Hegde M, Englert DL, Schrock S, Cohn WB, Vogt C, Wood TK, Manson MD, Jayaraman A. 2011. Chemotaxis to the quorum-sensing signal AI-2 requires the Tsr chemoreceptor and the periplasmic LsrB AI-2-binding protein. J Bacteriol 193:768-73.

12. Gonzalez JE, Keshavan ND. 2006. Messing with bacterial quorum sensing. Microbiol Mol Biol Rev 70:859-75.

13. Bassler BL. 1999. How bacteria talk to each other: regulation of gene expression by quorum sensing. Curr Opin Microbiol 2:582-7.

14. Bassler BL. 2002. Small talk. Cell-to-cell communication in bacteria. Cell 109:421-4.

15. Miller MB, Bassler BL. 2001. Quorum sensing in bacteria. Annu Rev Microbiol 55:165-99.

16. Papenfort K, Bassler BL. 2016. Quorum sensing signal-response systems in Gram-negative bacteria. Nat Rev Microbiol 14:576-88.

17. Fuqua WC, Winans SC, Greenberg EP. 1994. Quorum sensing in bacteria: the LuxR-LuxI family of cell density-responsive transcriptional regulators. J Bacteriol 176:269-75.

18. Waters CM, Bassler BL. 2005. Quorum sensing: cell-to-cell communication in bacteria. Annu Rev Cell Dev Biol 21:319-46.

19. Bassler BL, Greenberg EP, Stevens AM. 1997. Cross-species induction of luminescence in the quorum-sensing bacterium *Vibrio harveyi*. J Bacteriol 179:4043-5.

20. Miller ST, Xavier KB, Campagna SR, Taga ME, Semmelhack MF, Bassler BL, Hughson FM. 2004. *Salmonella typhimurium* recognizes a chemically distinct form of the bacterial quorum-sensing signal AI-2. Mol Cell 15:677-87.

21. Meijler MM, Hom LG, Kaufmann GF, McKenzie KM, Sun C, Moss JA, Matsushita M, Janda KD. 2004. Synthesis and biological validation of a ubiquitous quorum-sensing molecule. Angew Chem Int Ed Engl 43:2106-8.

22. Pereira CS, McAuley JR, Taga ME, Xavier KB, Miller ST. 2008. *Sinorhizobium meliloti*, a bacterium lacking the autoinducer-2 (AI-2) synthase, responds to AI-2 supplied by other bacteria. Mol Microbiol 70:1223-35.

23. Kavanaugh JS, Gakhar L, Horswill AR. 2011. The structure of LsrB from *Yersinia pestis* complexed with autoinducer-2. Acta Crystallogr Sect F Struct Biol Cryst Commun 67:1501-5.

24. Pereira CS, de Regt AK, Brito PH, Miller ST, Xavier KB. 2009. Identification of functional LsrB-like autoinducer-2 receptors. J Bacteriol 191:6975-87.

25. Chen X, Schauder S, Potier N, Van Dorsselaer A, Pelczer I, Bassler BL, Hughson FM. 2002. Structural identification of a bacterial quorum-sensing signal containing boron. Nature 415:545-9.

26. Pereira CS, Thompson JA, Xavier KB. 2013. AI-2-mediated signalling in bacteria. FEMS Microbiol Rev 37:156-81.

27. Rader BA, Campagna SR, Semmelhack MF, Bassler BL, Guillemin K. 2007. The quorum-sensing molecule autoinducer 2 regulates motility and flagellar morphogenesis in *Helicobacter pylori*. J Bacteriol 189:6109-17.

28. Rader BA, Wreden C, Hicks KG, Sweeney EG, Ottemann KM, Guillemin K. 2011. *Helicobacter pylori* perceives the quorum-sensing molecule AI-2 as a chemorepellent via the chemoreceptor TlpB. Microbiology 157:2445-55.

29. Anderson JK, Huang JY, Wreden C, Sweeney EG, Goers J, Remington SJ, Guillemin K. 2015. Chemorepulsion from the quorum signal autoinducer-2 promotes *Helicobacter pylori* biofilm dispersal. MBio 6:e00379.

30. Hammer BK, Bassler BL. 2003. Quorum sensing controls biofilm formation in *Vibrio cholerae*. Mol Microbiol 50:101-4.

31. Miller MB, Skorupski K, Lenz DH, Taylor RK, Bassler BL. 2002. Parallel quorum sensing systems converge to regulate virulence in *Vibrio cholerae*. Cell 110:303-14.

32. Auger S, Krin E, Aymerich S, Gohar M. 2006. Autoinducer 2 affects biofilm formation by *Bacillus cereus*. Appl Environ Microbiol 72:937-41.

33. Yu D, Zhao L, Xue T, Sun B. 2012. *Staphylococcus aureus* autoinducer-2 quorum sensing decreases biofilm formation in an *icaR*-dependent manner. BMC Microbiol 12:288.

34. Ahmed NA, Petersen FC, Scheie AA. 2007. AI-2 quorum sensing affects antibiotic susceptibility in *Streptococcus anginosus*. J Antimicrob Chemother 60:49-53.

35. Ahmed NA, Petersen FC, Scheie AA. 2009. AI-2/LuxS is involved in increased biofilm formation by *Streptococcus intermedius* in the presence of antibiotics. Antimicrob Agents Chemother 53:4258-63.

36. Redanz S, Standar K, Podbielski A, Kreikemeyer B. 2012. Heterologous expression of *sahH* reveals that biofilm formation is autoinducer-2-independent in *Streptococcus sanguinis* but is associated with an intact activated methionine cycle. J Biol Chem 287:36111-22.

37. Hosohama-Saito K, Kokubu E, Okamoto-Shibayama K, Kita D, Katakura A, Ishihara K. 2016. Involvement of *luxS* in biofilm formation by *Capnocytophaga ochracea*. PLoS One 11:e0147114.

38. Shao H, Lamont RJ, Demuth DR. 2007. Autoinducer 2 is required for biofilm growth of *Aggregatibacter (Actinobacillus) actinomycetemcomitans*. Infect Immun 75:4211-8.

39. Xavier KB, Bassler BL. 2005. Interference with AI-2-mediated bacterial cell-cell communication. Nature 437:750-3.

40. Silva AJ, Leitch GJ, Camilli A, Benitez JA. 2006. Contribution of hemagglutinin/protease and motility to the pathogenesis of El Tor biotype cholera. Infect Immun 74:2072-9.

41. Rickard AH, Palmer RJ, Jr., Blehert DS, Campagna SR, Semmelhack MF, Egland PG, Bassler BL, Kolenbrander PE. 2006. Autoinducer 2: a concentration-dependent signal for mutualistic bacterial biofilm growth. Mol Microbiol 60:1446-56.

42. McNab R, Ford SK, El-Sabaeny A, Barbieri B, Cook GS, Lamont RJ. 2003. LuxS-based signaling in *Streptococcus gordonii*: autoinducer 2 controls carbohydrate metabolism and biofilm formation with Porphyromonas gingivalis. J Bacteriol 185:274-84.

43. Cuadra-Saenz G, Rao DL, Underwood AJ, Belapure SA, Campagna SR, Sun Z, Tammariello S, Rickard AH. 2012. Autoinducer-2 influences interactions amongst pioneer colonizing streptococci in oral biofilms. Microbiology 158:1783-95.

44. Xavier KB, Bassler BL. 2005. Regulation of uptake and processing of the quorum-sensing autoinducer AI-2 in *Escherichia coli*. J Bacteriol 187:238-48.

45. Wang L, Li J, March JC, Valdes JJ, Bentley WE. 2005. *luxS*-dependent gene regulation in *Escherichia coli* K-12 revealed by genomic expression profiling. J Bacteriol 187:8350-60.

46. Taga ME, Semmelhack JL, Bassler BL. 2001. The LuxS-dependent autoinducer AI-2 controls the expression of an ABC transporter that functions in AI-2 uptake in *Salmonella typhimurium*. Mol Microbiol 42:777-93.

47. Wood TK, Gonzalez Barrios AF, Herzberg M, Lee J. 2006. Motility influences biofilm architecture in *Escherichia coli*. Appl Microbiol Biotechnol 72:361-7.

48. Gonzalez Barrios AF, Zuo R, Hashimoto Y, Yang L, Bentley WE, Wood TK. 2006. Autoinducer 2 controls biofilm formation in *Escherichia coli* through a novel motility quorum-sensing regulator (MqsR, B3022). J Bacteriol 188:305-16.

49. Maki N, Gestwicki JE, Lake EM, Kiessling LL, Adler J. 2000. Motility and chemotaxis of filamentous cells of *Escherichia coli*. J Bacteriol 182:4337-42.

50. Maddock JR, Shapiro L. 1993. Polar location of the chemoreceptor complex in the *Escherichia coli* cell. Science 259:1717-23.

51. Wadhams GH, Armitage JP. 2004. Making sense of it all: bacterial chemotaxis. Nat Rev Mol Cell Biol 5:1024-37.

52. Armitage JP. 1999. Bacterial tactic responses. Adv Microb Physiol 41:229-89.

53. Bansal T, Englert D, Lee J, Hegde M, Wood TK, Jayaraman A. 2007. Differential effects of epinephrine, norepinephrine, and indole on *Escherichia coli* O157:H7 chemotaxis, colonization, and gene expression. Infect Immun 75:4597-607.

54. Pasupuleti S, Sule N, Cohn WB, MacKenzie DS, Jayaraman A, Manson MD. 2014. Chemotaxis of *Escherichia coli* to norepinephrine (NE) requires conversion of NE to 3,4-dihydroxymandelic acid. J Bacteriol 196:3992-4000.

55. Huang JY, Sweeney EG, Sigal M, Zhang HC, Remington SJ, Cantrell MA, Kuo CJ, Guillemin K, Amieva MR. 2015. Chemodetection and destruction of host urea allows *Helicobacter pylori* to locate the epithelium. Cell Host Microbe 18:147-56.

56. Rivera-Chavez F, Winter SE, Lopez CA, Xavier MN, Winter MG, Nuccio SP, Russell JM, Laughlin RC, Lawhon SD, Sterzenbach T, Bevins CL, Tsolis RM, Harshey R, Adams LG, Baumler AJ. 2013. *Salmonella* uses energy taxis to benefit from intestinal inflammation. PLoS Pathog 9:e1003267.

57. Manson MD, Boos W, Bassford PJ, Jr., Rasmussen BA. 1985. Dependence of maltose transport and chemotaxis on the amount of maltose-binding protein. J Biol Chem 260:9727-33.

58. Hazelbauer GL, Adler J. 1971. Role of the galactose binding protein in chemotaxis of *Escherichia coli* toward galactose. Nat New Biol 230:101-4.

59. Aksamit RR, Koshland DE, Jr. 1974. Identification of the ribose binding protein as the receptor for ribose chemotaxis in *Salmonella typhimurium*. Biochemistry 13:4473-8.

60. Manson MD, Blank V, Brade G, Higgins CF. 1986. Peptide chemotaxis in *E. coli* involves the Tap signal transducer and the dipeptide permease. Nature 321:253-6.

61. Liu X, Parales RE. 2008. Chemotaxis of *Escherichia coli* to pyrimidines: a new role for the signal transducer tap. J Bacteriol 190:972-9.

62. Bibikov SI, Miller AC, Gosink KK, Parkinson JS. 2004. Methylation-independent aerotaxis mediated by the *Escherichia coli* Aer protein. J Bacteriol 186:3730-7.

63. Borziak K, Fleetwood AD, Zhulin IB. 2013. Chemoreceptor gene loss and acquisition via horizontal gene transfer in *Escherichia coli*. J Bacteriol 195:3596-602.

64. Hazelbauer GL, Falke JJ, Parkinson JS. 2008. Bacterial chemoreceptors: high-performance signaling in networked arrays. Trends Biochem Sci 33:9-19.

65. Costerton JW. 1995. Overview of microbial biofilms. J Ind Microbiol 15:137-40.

66. Donlan RM. 2002. Biofilms: microbial life on surfaces. Emerg Infect Dis 8:881-90.

67. Davey ME, O'Toole G A. 2000. Microbial biofilms: from ecology to molecular genetics. Microbiol Mol Biol Rev 64:847-67.

68. Hall-Stoodley L, Costerton JW, Stoodley P. 2004. Bacterial biofilms: from the natural environment to infectious diseases. Nat Rev Microbiol 2:95-108.

69. Donlan RM, Costerton JW. 2002. Biofilms: survival mechanisms of clinically relevant microorganisms. Clin Microbiol Rev 15:167-93.

70. Zobell CE. 1943. The effect of solid surfaces upon bacterial activity. J Bacteriol 46:39-56.

71. Cairns LS, Marlow VL, Bissett E, Ostrowski A, Stanley-Wall NR. 2013. A mechanical signal transmitted by the flagellum controls signalling in *Bacillus subtilis*. Mol Microbiol 90:6-21.

72. Guttenplan SB, Shaw S, Kearns DB. 2013. The cell biology of peritrichous flagella in *Bacillus subtilis*. Mol Microbiol 87:211-29.

73. Belas R. 2014. Biofilms, flagella, and mechanosensing of surfaces by bacteria. Trends Microbiol 22:517-27.

74. O'Toole GA, Wong GC. 2016. Sensational biofilms: surface sensing in bacteria. Curr Opin Microbiol 30:139-46.

75. Otto K, Silhavy TJ. 2002. Surface sensing and adhesion of *Escherichia coli* controlled by the Cpx-signaling pathway. Proc Natl Acad Sci U S A 99:2287-92.

76. Monds RD, Newell PD, Gross RH, O'Toole GA. 2007. Phosphate-dependent sformation by controlling secretion of the adhesin LapA. Mol Microbiol 63:656-79.

77. Kolenbrander PE, London J. 1993. Adhere today, here tomorrow: oral bacterial adherence. J Bacteriol 175:3247-52.

78. Caiazza NC, O'Toole GA. 2004. SadB is required for the transition from reversible to irreversible attachment during biofilm formation by *Pseudomonas aeruginosa* PA14. J Bacteriol 186:4476-85.

79. Lawrence JR, Delaquis PJ, Korber DR, Caldwell DE. 1987. Behavior of *Pseudomonas fluorescens* within the Hydrodynamic Boundary-Layers of Surface Microenvironments. Microbial Ecology 14:1-14.

80. Guttenplan SB, Kearns DB. 2013. Regulation of flagellar motility during biofilm formation. FEMS Microbiol Rev 37:849-71.

81. Wood TK. 2009. Insights on *Escherichia coli* biofilm formation and inhibition from whole-transcriptome profiling. Environ Microbiol 11:1-15.

82. Karatan E, Watnick P. 2009. Signals, regulatory networks, and materials that build and break bacterial biofilms. Microbiol Mol Biol Rev 73:310-47.

83. Pratt LA, Kolter R. 1998. Genetic analysis of *Escherichia coli* biofilm formation: roles of flagella, motility, chemotaxis and type I pili. Mol Microbiol 30:285-93.

84. Genevaux P, Muller S, Bauda P. 1996. A rapid screening procedure to identify mini-Tn10 insertion mutants of *Escherichia coli* K-12 with altered adhesion properties. FEMS Microbiol Lett 142:27-30.

85. Vigeant MA, Ford RM, Wagner M, Tamm LK. 2002. Reversible and irreversible adhesion of motile *Escherichia coli* cells analyzed by total internal reflection aqueous fluorescence microscopy. Appl Environ Microbiol 68:2794-801.

86. Alexandre G. 2015. Chemotaxis control of transient cell aggregation. J Bacteriol 197:3230-7.

87. Sourjik V, Wingreen NS. 2012. Responding to chemical gradients: bacterial chemotaxis. Curr Opin Cell Biol 24:262-8.

88. Tuson HH, Weibel DB. 2013. Bacteria-surface interactions. Soft Matter 9:4368-4380.

89. Nguyen Y, Sperandio V. 2012. Enterohemorrhagic *E. coli* (EHEC) pathogenesis. Front Cell Infect Microbiol 2:90.

90. Martinez-Medina M, Naves P, Blanco J, Aldeguer X, Blanco JE, Blanco M, Ponte C, Soriano F, Darfeuille-Michaud A, Garcia-Gil LJ. 2009. Biofilm formation as a novel phenotypic feature of adherent-invasive *Escherichia coli* (AIEC). BMC Microbiol 9:202.

91. Parkinson JS, Houts SE. 1982. Isolation and behavior of *Escherichia coli* deletion mutants lacking chemotaxis functions. J Bacteriol 151:106-13.

92. Hansen MC, Palmer RJ, Jr., Udsen C, White DC, Molin S. 2001. Assessment of GFP fluorescence in cells of *Streptococcus gordonii* under conditions of low pH and low oxygen concentration. Microbiology 147:1383-91.

93. Baba T, Ara T, Hasegawa M, Takai Y, Okumura Y, Baba M, Datsenko KA, Tomita M, Wanner BL, Mori H. 2006. Construction of *Escherichia coli* K-12 in-frame, single-gene knockout mutants: the Keio collection. Mol Syst Biol 2:2006 0008.

94. Thomason LC, Costantino N, Court DL. 2007. *E. coli* genome manipulation by P1 transduction. Curr Protoc Mol Biol Chapter 1:Unit 1 17.

95. Datsenko KA, Wanner BL. 2000. One-step inactivation of chromosomal genes in *Escherichia coli* K-12 using PCR products. Proc Natl Acad Sci U S A 97:6640-5.

96. Pougach K, Semenova E, Bogdanova E, Datsenko KA, Djordjevic M, Wanner BL, Severinov K. 2010. Transcription, processing and function of CRISPR cassettes in *Escherichia coli*. Mol Microbiol 77:1367-79.

97. Reisner A, Krogfelt KA, Klein BM, Zechner EL, Molin S. 2006. *In vitro* biofilm formation of commensal and pathogenic *Escherichia coli* strains: impact of environmental and genetic factors. J Bacteriol 188:3572-81.

98. Schindelin J, Rueden CT, Hiner MC, Eliceiri KW. 2015. The ImageJ ecosystem: An open platform for biomedical image analysis. Mol Reprod Dev 82:518-29.

99. Merritt JH, Kadouri DE, O'Toole GA. 2005. Growing and analyzing static biofilms. Curr Protoc Microbiol Chapter 1:Unit 1B 1.

100. Christensen GD, Simpson WA, Younger JJ, Baddour LM, Barrett FF, Melton DM, Beachey EH. 1985. Adherence of coagulase-negative *Saphylococci* to

plastic tissue culture plates: a quantitative model for the adherence of *Staphylococci* to medical devices. J Clin Microbiol 22:996-1006.

101. Taga ME. 2005. Methods for analysis of bacterial autoinducer-2 production. Curr Protoc Microbiol Chapter 1:Unit 1C 1.

102. Adler J. 1973. A method for measuring chemotaxis and use of the method to determine optimum conditions for chemotaxis by *Escherichia coli*. J Gen Microbiol 74:77-91.

103. Zhou Y, Smith DR, Hufnagel DA, Chapman MR. 2013. Experimental manipulation of the microbial functional amyloid called curli. Methods Mol Biol 966:53-75.

104. Long T, Tu KC, Wang Y, Mehta P, Ong NP, Bassler BL, Wingreen NS. 2009. Quantifying the integration of quorum-sensing signals with single-cell resolution. PLoS Biol 7:e68.

105. Pantanella F, Valenti P, Natalizi T, Passeri D, Berlutti F. 2013. Analytical techniques to study microbial biofilm on abiotic surfaces: pros and cons of the main techniques currently in use. Ann Ig 25:31-42.

106. Karygianni L, Follo M, Hellwig E, Burghardt D, Wolkewitz M, Anderson A, Al-Ahmad A. 2012. Microscope-based imaging platform for large-scale analysis of oral biofilms. Appl Environ Microbiol 78:8703-11.

107. Lawrence JR, Korber DR, Hoyle BD, Costerton JW, Caldwell DE. 1991. Optical sectioning of microbial biofilms. J Bacteriol 173:6558-67.

108. Savageau MA. 1983. *Escherichia coli* habitats, cell-types, and molecular mechanisms of gene-control. American Naturalist 122:732-744.

109. Winfield MD, Groisman EA. 2003. Role of nonhost environments in the lifestyles of *Salmonella* and *Escherichia coli*. Applied and Environmental Microbiology 69:3687-3694.

110. van Elsas JD, Semenov AV, Costa R, Trevors JT. 2011. Survival of *Escherichia coli* in the environment: fundamental and public health aspects. ISME J 5:173-83.

111. Taga ME, Xavier KB. 2011. Methods for analysis of bacterial autoinducer-2 production. Curr Protoc Microbiol Chapter 1:Unit1C 1.

112. Turovskiy Y, Chikindas ML. 2006. Autoinducer-2 bioassay is a qualitative, not quantitative method influenced by glucose. J Microbiol Methods 66:497-503.

113. Pereira CS, Santos AJ, Bejerano-Sagie M, Correia PB, Marques JC, Xavier KB. 2012. Phosphoenolpyruvate phosphotransferase system regulates detection and processing of the quorum sensing signal autoinducer-2. Mol Microbiol 84:93-104.

114. Beloin C, Roux A, Ghigo JM. 2008. *Escherichia coli* biofilms. Curr Top Microbiol Immunol 322:249-89.

115. Cookson AL, Cooley WA, Woodward MJ. 2002. The role of type 1 and curli fimbriae of Shiga toxin-producing *Escherichia coli* in adherence to abiotic surfaces. Int J Med Microbiol 292:195-205.

116. Uhlich GA, Cooke PH, Solomon EB. 2006. Analyses of the red-dry-rough phenotype of an *Escherichia coli* O157:H7 strain and its role in biofilm formation and resistance to antibacterial agents. Appl Environ Microbiol 72:2564-72.

117. Barnhart MM, Chapman MR. 2006. Curli biogenesis and function. Annu Rev Microbiol 60:131-47.

118. Kikuchi T, Mizunoe Y, Takade A, Naito S, Yoshida S. 2005. Curli fibers are required for development of biofilm architecture in *Escherichia coli* K-12 and enhance bacterial adherence to human uroepithelial cells. Microbiol Immunol 49:875-84.

119. Dudin O, Geiselmann J, Ogasawara H, Ishihama A, Lacour S. 2014. Repression of flagellar genes in exponential phase by CsgD and CpxR, two crucial modulators of *Escherichia coli* biofilm formation. J Bacteriol 196:707-15.

120. Park S, Wolanin PM, Yuzbashyan EA, Silberzan P, Stock JB, Austin RH. 2003. Motion to form a quorum. Science 301:188.

121. Laganenka L, Colin R, Sourjik V. 2016. Chemotaxis towards autoinducer 2 mediates autoaggregation in *Escherichia coli*. Nat Commun 7:12984.

122. Vendeville A, Winzer K, Heurlier K, Tang CM, Hardie KR. 2005. Making 'sense' of metabolism: autoinducer-2, LuxS and pathogenic bacteria. Nat Rev Microbiol 3:383-96.

123. Gao M, Zheng H, Ren Y, Lou R, Wu F, Yu W, Liu X, Ma X. 2016. A crucial role for spatial distribution in bacterial quorum sensing. Sci Rep 6:34695.

124. Mesibov R, Adler J. 1972. Chemotaxis toward amino acids in *Escherichia coli*. J Bacteriol 112:315-26.

125. Adler J, Hazelbauer GL, Dahl MM. 1973. Chemotaxis toward sugars in *Escherichia coli*. J Bacteriol 115:824-47.

126. Adler J, Epstein W. 1974. Phosphotransferase-system enzymes as chemoreceptors for certain sugars in *Escherichia coli* chemotaxis. Proc Natl Acad Sci U S A 71:2895-9.

127. Tso WW, Adler J. 1974. Negative chemotaxis in *Escherichia coli*. J Bacteriol 118:560-76.

128. Adler J. 2011. My life with nature. Annu Rev Biochem 80:42-70.

129. Hazelbauer GL. 2012. Bacterial chemotaxis: the early years of molecular studies. Annu Rev Microbiol 66:285-303.

130. Falke JJ, Bass RB, Butler SL, Chervitz SA, Danielson MA. 1997. The two-component signaling pathway of bacterial chemotaxis: a molecular view of signal transduction by receptors, kinases, and adaptation enzymes. Annu Rev Cell Dev Biol 13:457-512.

131. Falke JJ, Hazelbauer GL. 2001. Transmembrane signaling in bacterial chemoreceptors. Trends Biochem Sci 26:257-65.

132. Lu L, Hume ME, Pillai SD. 2004. Autoinducer-2-like activity associated with foods and its interaction with food additives. J Food Prot 67:1457-62.

133. Thompson JA, Oliveira RA, Djukovic A, Ubeda C, Xavier KB. 2015. Manipulation of the quorum sensing signal AI-2 affects the antibiotic-treated gut microbiota. Cell Rep 10:1861-71.

134. Kondoh H, Ball CB, Adler J. 1979. Identification of a methyl-accepting chemotaxis protein for the ribose and galactose chemoreceptors of *Escherichia coli*. Proc Natl Acad Sci U S A 76:260-4.

135. Zhang Y, Gardina PJ, Kuebler AS, Kang HS, Christopher JA, Manson MD. 1999. Model of maltose-binding protein/chemoreceptor complex supports intrasubunit signaling mechanism. Proc Natl Acad Sci U S A 96:939-44.

136. Zhang Y, Conway C, Rosato M, Suh Y, Manson MD. 1992. Maltose chemotaxis involves residues in the N-terminal and C-terminal domains on the same face of maltose-binding protein. J Biol Chem 267:22813-20.

137. Gardina P, Conway C, Kossman M, Manson M. 1992. Aspartate and maltose-binding protein interact with adjacent sites in the Tar chemotactic signal transducer of *Escherichia coli*. J Bacteriol 174:1528-36.

138. Li M, Hazelbauer GL. 2004. Cellular stoichiometry of the components of the chemotaxis signaling complex. J Bacteriol 186:3687-94.

139. Zhu J, Pei D. 2008. A LuxP-based fluorescent sensor for bacterial autoinducer II. ACS Chem Biol 3:110-9.

140. Sezonov G, Joseleau-Petit D, D'Ari R. 2007. *Escherichia coli* physiology in Luria-Bertani broth. J Bacteriol 189:8746-9.

141. Ascenso OS, Marques JC, Santos AR, Xavier KB, Ventura MR, Maycock CD. 2011. An efficient synthesis of the precursor of AI-2, the signalling molecule for inter-species quorum sensing. Bioorg Med Chem 19:1236-41.

142. Neu HC, Heppel LA. 1965. The release of enzymes from *Escherichia coli* by osmotic shock and during the formation of spheroplasts. J Biol Chem 240:3685-92.

143. Manns JM. 2011. SDS-Polyacrylamide Gel Electrophoresis (SDS-PAGE) of Proteins. Current Protocols in Microbiology 22:A.3M.1–A.3M.13.

144. Kalinin Y, Neumann S, Sourjik V, Wu M. 2010. Responses of *Escherichia coli* bacteria to two opposing chemoattractant gradients depend on the chemoreceptor ratio. J Bacteriol 192:1796-800.

145. Gestwicki JE, Kiessling LL. 2002. Inter-receptor communication through arrays of bacterial chemoreceptors. Nature 415:81-4.

146. Martinez-Medina M, Garcia-Gil LJ. 2014. *Escherichia coli* in chronic inflammatory bowel diseases: An update on adherent invasive *Escherichia coli* pathogenicity. World J Gastrointest Pathophysiol 5:213-27.

147. Quinones B, Miller WG, Bates AH, Mandrell RE. 2009. Autoinducer-2 production in *Campylobacter jejuni* contributes to chicken colonization. Appl Environ Microbiol 75:281-5.

148. Haag LM, Fischer A, Otto B, Plickert R, Kuhl AA, Gobel UB, Bereswill S, Heimesaat MM. 2012. Intestinal microbiota shifts towards elevated commensal *Escherichia coli* loads abrogate colonization resistance against *Campylobacter jejuni* in mice. PLoS One 7:e35988.

149. Adler L, Alter T, Sharbati S, Golz G. 2015. The signalling molecule autoinducer-2 is not internalised in *Campylobacter jejuni*. Berl Munch Tierarztl Wochenschr 128:111-6.